This is a preprint, the final version is subject to change, of the American Mineralogist (MSA)
Cite as Authors (Year) Title. American Mineralogist, in press.
DOI: https://doi.org/10.2138/am-2020-7383

Revision 2

Direct evidence for the source of uranium in the Baiyanghe deposit from accessory mineral alteration in the Yangzhuang granite porphyry, Xinjiang Province, Northwest China

LONG ZHANG[1,2,3], XIAOFENG LI[1,2,3,*], GUO WANG[4] AND MOU WANG[4]

[1]Key Laboratory of Mineral Resources, Institute of Geology and Geophysics, Chinese Academy of Sciences, Beijing 100029, China

[2]Institutions of Earth Science, Chinese Academy of Sciences, Beijing 100029, China

[3]College of Earth and Planetary Sciences, University of Chinese Academy of Sciences, Beijing 100049, China

[4]No. 216 Geological Survey, China National Nuclear Corporation, Urumqi 830011, China

* Corresponding author at: Institute of Geology and Geophysics, Chinese Academy of Sciences, No. 19, Beitucheng Western Road, Chaoyang District, Beijing 100029, China.
E-mail address: xiaofengli@mail.iggcas.ac.cn

This is a preprint, the final version is subject to change, of the American Mineralogist (MSA)
Cite as Authors (Year) Title. American Mineralogist, in press.
DOI: https://doi.org/10.2138/am-2020-7383

ABSTRACT

Circumstantial evidence for the sources of uranium in ore deposits may be drawn from the study of deposit geochemistry and mineralogy. However, direct evidence supporting uranium leaching from source rocks has rarely been found. This study investigates the source of uranium in the Baiyanghe deposit in the Xiemisitai Mountains, NW China. The main uranium ore bodies occur as fracture-fillings along contact zones between the Yangzhuang granite porphyry and the Devonian volcanic rocks. Zircon, thorite, columbite-(Mn), and bastnäsite are the dominant accessory minerals that host uranium in the granite porphyry. *In situ* columbite-(Mn) LA-ICP-MS U-Pb dating yields a weighted mean $^{206}Pb/^{238}U$ age of 310 ± 4 Ma, suggesting that the Yangzhuang granite porphyry was emplaced during the Late Carboniferous. Back-scattered electron (BSE) images reveal that various degrees of alteration of these same accessory minerals may be observed in the granite porphyry, and the altered domains of these minerals have lower BSE intensities compared to the unaltered domains. Results indicate that the altered domains of zircon grains have lower concentrations of Zr, Si, and U, and higher concentrations of Y, Fe, Ca, and P relative to the unaltered domains, and the altered domains of columbite-(Mn) grains are enriched in Ti and Fe, and are depleted in Nb, Ta, Mn, U, and Zr. The altered domains of thorite grains have higher concentrations of Zr, Fe, Ca, Nb, and P, and lower Th and U compared to those of the relict domains. The

petrochemical data indicate that the granite porphyry experienced losses in U, Be, F, Ba, Sr, Pb, Zr, Mo, Nb, Ta, and Hf during alteration. These results suggest that the past-magmatic hydrothermal fluids might be responsible for the mobilization of uranium form minerals in the granite porphyry. It is concluded that U-bearing accessory minerals in the granite porphyry were the primary source of uranium, and that post-magmatic hydrothermal processes caused remobilization and significant localized enrichment of the uranium to form high-grade ores as fracture-fillings along its contacts.

Keywords: U-bearing accessory minerals, Hydrothermal alteration, Element maps, Uranium source, Yangzhuang granite porphyry, Baiyanghe volcanic deposit

59 # INTRODUCTION

60 Uranium deposits may be divided into diverse types (i.e., sandstone, vein, volcanic,
61 unconformity, metasomatic, and phosphorite) based on the sources and the environment
62 of formation for uranium ore minerals (Dahlkamp 1993). However, the majority of
63 deposits are of post-magmatic hydrothermal origin (Cuney and Kyser 2008; Hu et al.
64 2008; Nash 2010; Cuney 2014). In many examples of secondary-enrichment researchers
65 have proposed regions (or rocks) that may represent the sources of uranium in the
66 deposits, but much of the evidence is circumstantial and based on the deposit
67 geochemistry and mineralogy (e.g., Cuney and Mathieu 2000; Hecht and Cuney 2000;
68 Mathieuet al. 2001; Chabiron et al. 2003; Tartèse et al. 2013; Christiansen et al. 2015;
69 Bonnetti et al. 2017). Few studies provide direct evidence supporting uranium leaching
70 from minerals in the source rocks (e.g., McGloin et al. 2016). In granitoids, uranium is
71 mainly hosted in accessory phases such as uraninite, zircon, thorite, allanite, and
72 monazite (Pagel 1982; Cuney and Friedrich 1987; Bea 1996; Förster 1999; Cuney 2009,
73 2014). Therefore, micro-scale leaching of uranium from primary U-bearing phases may
74 be a key step in the formation of hydrothermal uranium deposits (Nasdala et al. 2010;
75 Seydoux-Guillaume et al. 2015; McGloin et al. 2016).

76 The Baiyanghe deposit, located in the Xiemisitai Mountains, NW China (Fig. 1), is
77 the largest volcanogenic beryllium deposit in Asia (Li et al. 2015), and provides an

opportunity to investigate the source of uranium in ore deposits. In the Baiyanghe deposit, a series of uranium occurrences are spatially but not temporally associated with the Yangzhuang granite porphyry (Fig. 2a, Ma et al. 2010; Li et al. 2015; Zhang et al. 2019). The uranium-beryllium ore bodies mainly occur as fracture-fillings along contact zones between the Yangzhuang granite porphyry and the Devonian volcanic rocks (Wang et al. 2012; Li et al. 2015). The Yangzhuang granite porphyry formed at 313.4 ± 2.3 Ma (LA-ICP-MS zircon U-Pb age, Zhang and Zhang 2014), whereas the Baiyanghe uranium mineralization occurred at 229 ± 26 Ma (uraninite U-Pb isochron age, Xia 2019). Whole-rock geochemistry data indicate that the Yangzhuang granite porphyry has much higher concentrations of U, Th, Nb, Ta, Be, and F compared with the volcanic rocks of the basement in this area (Mao et al. 2014; Zhang and Zhang 2014; Zhang et al. 2019). This makes the granite a potential source of uranium that formed the Baiyanghe uranium deposit (Ma et al. 2010; Mao et al. 2013; Li et al. 2015; Yi 2016; Zhang et al. 2019), provided that appropriate hydrothermal fluids may interact with and leach uranium from the Yangzhuang granite porphyry. Element mapping is a useful tool for obtaining direct evidence for the mobilization of some elements from minerals during hydrothermal alteration and could thereby help to determine which regions are the primary sources of uranium in ore deposits (McGloin et al. 2016). Whether the Devonian volcanic rocks also represent a possible source of uranium in the Baiyanghe deposit has been not been previously addressed. To address the source of uranium in the Baiyanghe deposit, we

present textural and compositional features of U-bearing accessory minerals in the granite porphyry, and their corresponding alteration products. Furthermore, whole-rock mass-balance calculations are made to assess the chemical gains and losses in mass transfer during the alteration process.

GEOLOGICAL SETTING

Regional geology

The Baiyanghe deposit is located in the Xiemisitai Mountains of the northwest margin of the West Junggar, NW China (Mao et al. 2014; Zhang and Zhang 2014) (Fig. 1). The West Junggar, located in the northern Xinjiang Uygur Autonomous Region, geographically, may be divided into northern and southern parts (Fig. 1) (Xu et al. 2012). The northern West Junggar mainly includes the NW-trending Zharma-Saur and Boshchekul-Chingiz volcanic arcs from the north to south (Windley et al. 2007; Xiao et al. 2008; Chen et al. 2010). The Boshchekul-Chingiz volcanic arc in the Xiemisitai, Saier, and Sharbuerti Mountains consists of the Middle Ordovician to Silurian marine volcanic clastic and pyrolcastic sediments, Silurian to Early Devonian calc-alkaline and alkaline magmatism (Chen et al. 2010, 2015, 2019; Shen et al. 2012; Choulet et al. 2012; Yang et al. 2014; Yin et al. 2017, 2018).

The Xiemisitai Mountains are dominated by a suite of intermediate to felsic volcanic and intrusive rocks, with minor amounts of the Late Carboniferous-Middle Permian granite, granite porphyry, and diorite (Chen et al. 2010, 2015, 2019; Shen et al. 2012; Yin et al. 2017, 2018). The volcanic rocks include andesite, rhyolite, and their pyroclastic equivalents; the subvolcanic units are felsite and granite porphyry. These rocks of the Xiemisitai Mountains were formed during the Late Silurian to Early Devonian and were likely generated in a normal arc-related setting (Shen et al. 2012; Yang et al. 2014). The Baiyanghe deposit is located on the southern border of the middle part of the Xiemisitai Mountains. Stratigraphic sequences in the Baiyanghe deposit include the Early Devonian Tarbagatay Group of intermediate-felsic volcanic and pyroclastic rocks with minor mafic tuff, the Early Carboniferous Hebukehe Group of shale, limestone, siliceous shale, sandstone, and conglomerate, as well as the Early Carboniferous Heishantou Group of mafic-intermediate volcanic and pyroclastic rocks (Ma et al. 2012; Wang et al. 2012; Zhang and Zhang 2014; Li et al. 2015).

Geology of the Baiyanghe deposit

The Baiyanghe U-Be mineralization is closely associated with the Yangzhuang granite porphyry (Fig. 2a) (Li et al. 2015). It was intruded along the EW-trending Yangzhuang fault in the south and the Devonian volcanic rocks in the north and the east (Li et al. 2015; Zhang et al. 2019). The Baiyanghe deposit has three types of ores. These

are: U-type, Be-type, and Be-U-Mo-type (Ma et al. 2010; Wang et al. 2012; Li et al. 2015). These ores occur either separately or show cross-cutting relationships (Li et al. 2015). The main ore bodies in the Baiyanghe deposit occur as fracture-fillings along contact zones between the Yangzhuang granite porphyry and the Devonian volcanic rocks (Fig. 2b). Detailed field observations show that most of the contact zones associated with the U-Be mineralization are fractured and have abundant fluorite (Fig. 3a). The fracture zones may also be found within the granite porphyry and have purple fluorite (Fig. 3b). These observations suggest that the Baiyanghe U-Be mineralization might have occurred after the emplacement of the Yangzhuang granite porphyry. In the field, several diorite and diabase dykes intruded the Baiyanghe deposit (Fig. 2a). They were emplaced during the Early Permian to Late Triassic (Ma et al. 2010; Miao et al. 2019). Miao et al. (2019) suggested that the diabase dykes in the Baiyanghe deposit were probably derived from an ocean-island basalts (OIB)-like mantle source and associated with a mantle plume tectonic setting.

The uranium ore minerals in the Baiyanghe deposit are dominated by uraninite (Fig. 3c). The principal Be-ore mineral is bertrandite ($Be_4Si_2O_7(OH)_2$) (Fig. 3d), which occurs solely as submicroscopic grains admixed with fluorite (Li et al. 2015; Zhang et al. 2019). The close association of uraninite, bertrandite and fluorite might support co-precipitation (Zhang et al. 2019). The gangue minerals are quartz, albite, K-feldspar, muscovite,

chlorite, and fluorite. The hydrothermal alteration associated with uranium mineralization includes fluoritization, hematitization, silicification, chloritization, and carbonatization (Zhang et al. 2019).

SAMPLING AND ANALYTICAL METHODS

Sample preparation

Thirty-five whole rock samples collected from drill cores and outcrops were used in this study, and the sample descriptions are presented in Supplementary Table 1. These samples were used for whole-rock major and trace element analyses, petrographic observations by reflected and transmitted light microscopy and back-scattered electron imaging, quantitative analyses and element mapping of U-bearing accessory minerals by electron probe microanalyzer (EPMA), and *in situ* trace element analyses of mica and U-Pb dating of columbite-(Mn) using laser ablation-inductively coupled plasma-mass spectrometry (LA-ICP-MS).

Whole-rock major and trace element analyses

Whole-rock major and trace elements were analyzed at the National Research Center for Geoanalysis, Chinese Academy of Geological Sciences in Beijing, China. Major elements of whole rocks were analyzed by wavelength-dispersive X-ray fluorescence spectrometry of fused glass beads using a Philips PW2404 spectrometer.

Analytical relative errors were < 2 %. The detailed analytical technique is similar to that described in Zhang et al. (2019). Trace elements were determined by a Finnigan MAT Element I HR-ICP-MS. Pure element standard solutions were used for external calibration and BHVO-1 and SY-4 were used as reference materials. The uncertainties of the ICP-MS analyses are estimated to be better than ± 5% for most trace elements with concentrations > 10 ppm, and ± 10% for those < 10 ppm. The major and trace elements of the least-altered and altered granite porphyry and tuff from the Baiyanghe deposit are provided in Supplementary Table 2.

Electron probe microprobe analysis

Back-scattered electron imaging, quantitative analyses of mica and U-bearing minerals from the Yangzhuang granite porphyry, and element mapping were performed using a JEOL JXA-8230 electron probe microanalyzer at the Key Laboratory of Metallogeny and Mineral Assessment, Chinese Academy of Geological Sciences, Beijing, China. The operating conditions for the U-bearing accessory mineral samples were 15 kV accelerating voltage, a beam current of 50 nA, with variable counting times between 10 and 100 s and between 5 and 50 s in the peak and background, respectively. The beam diameter ranged from 1 to 5 μm and a ZAF matrix-correction was applied during data reduction. Elements Si, Ti, Al, Fe, Mg, Mn, Mo, P, U, Th, Hf, Zr, Pb, Mg, Y, Cr, Ca, Na, Sn, K, F, Cl, and rare earth elements (REEs) were analyzed. The following standards and

crystals were used for microanalyses: jadeite (Na-Kα, TAP; Al-Kα, TAP; Si-Kα, PETJ); forsterite (Mg-Kα, TAP); topaz (F-Kα, TAP); K-feldspar (K-Kα, PETG); wollastonite (Ca-Kα, PETH); hematite, (Fe-Kα, LIF); rutile (Ti-Kα, LIF); apatite (P-Kα, PETJ); Cr_2O_3 (Cr-Kα, LIFH); MnO (Mn-Kα, LIFH); V_2O_5 (V-Kα, LIFH); and NaCl (Cl-Kα, PETH). For REE, synthetic rare earth pentaphosphate crystals were used as standards. The EPMA chemical compositions of feldspars and accessory minerals (including zircon, columbite-(Mn), and thorite) are provided in Supplementary Table 3 and Table 4, respectively.

The operating conditions for element mapping were 15 kv accelerating voltage with 100 nA beam current, and 50 ms dwell time for qualitative element maps of the distribution of U, Th, Zr, Ca, Si, Fe, Mo, Nb, Ta, Mn, Ti, P, Hf, F, Y, and REEs were collected. The element maps (Figs. 7, 8, and 11) were obtained by stage-mapping over a frame size of 250 or 150 μm using an image size of 500 pixels with each pixel representing a step size of 0.5 or 0.3 μm respectively (Fig. 9).

Laser ablation-inductively coupled plasma-mass spectrometry analyses

In situ trace element analyses of mica were obtained using an Agilent 7500a quadrupole inductively coupled plasma mass spectrometer (ICP-MS) coupled to a 193nm ArF Excimer laser ablation system at the Institute of Geology and Geophysics, Chinese

Academy of Sciences, Beijing, China. All analyses were obtained from polished thin sections. Following a 40-s background analysis, the mica samples were ablated for 60 s at a repetition rate of 8 Hz, energy density of ~10 J/cm^2, and a crater beam of 50 μm. The following isotopes were measured: ^{7}Li, ^{9}Be, ^{45}Sc, ^{51}V, ^{53}Cr, ^{85}Rb, ^{89}Y, ^{93}Nb, ^{95}Mo, ^{133}Cs, ^{139}La, ^{140}Ce, ^{181}Ta, ^{232}Th, and ^{238}U. The detailed analytical technique is similar to that described in Xie et al. (2008). NIST610, NIST612, and BIR-1G were used as external standards, and ^{29}Si was used as an internal standard. Data reduction and concentration calculations were performed using the program of Glitter (Griffin et al. 2008). In situ trace-element analytical results and limits of detection of the trace element concentrations for mica and columbite-(Mn) are listed in Supplementary Table 5 and Table 6, respectively.

U-Pb geochronology of columbite-(Mn) was also carried out via LA-ICP-MS at the same laboratory and with similar operating condition. Samples were analyzed using a spot size of 35 μm, a repetition rate of 6 Hz and Coltan 139 (Gäbler et al. 2011; Che et al. 2015) was used as external standard reference. Trace elements in columbite-(Mn) were calibrated against multiple-reference standards (NIST 610) combined with internal standardization. Coltan 139 was analyzed twice for every five analyses. Each spot analysis incorporated a background acquisition of approximately 20 s, followed by 40 s sample data acquisition. The concordia and weighted mean U-Pb ages were calculated by

using ISOPLOT/EX 4.15 software package. Trace element compositions were also calculated by GLITTER 4.0, with ^{55}Mn as the internal standard and NIST 610 as an external reference material. The detailed analytical technique was described by Che et al. (2015). The LA-ICP-MS U-Pb data for Coltan 139 and columbite-(Mn) are presented in Supplementary Table 7.

RESULTS

Petrography

Petrography of the granite porphyry and tuff. The Yangzhuang granite porphyry exhibits a porphyritic texture with quartz and K-feldspar phenocrysts (Fig. 4a). Anhedral quartz and slightly altered euhedral K-feldspar phenocrysts were identified in thin section. The matrix is mainly composed of quartz, K-feldspar, plagioclase, and zinnwaldite (Fig. 4b). The accessory mineral assemblage consists of zircon, thorite, columbite-(Mn), bastnäsite, fluorite, magnetite, and minor ilmenite (Figs. 4e-g). The wall-rock alteration of the granite porphyry has been investigated by Fayek and Shabaga (2011), Xu et al. (2017), and Zhang et al. (2019). These studies suggest that sericitic alteration is pervasive, and chloritization, albitization, hematitzation, and fluorination may also be found. In the altered samples of the granite porphyry, except for the widespread argillization of K-feldspar (Fig. 4c), K-feldspar phenocrysts were also partially replaced by albite (Fig. 4d). The least-altered crystal tuff is composed of quartz and K-feldspar phenocrysts and

lithic fragments in a fine-grained matrix comprising quartz, feldspar, sericite, and some glass (Fig. 4h). The major alteration minerals are chlorite (Fig. 4i), illite, fluorite, and epidote. In addition, purple fluorite was observed in the altered sample (BY-1) (Fig. 4i).

Textures of U-bearing accessory minerals. Detailed petrographic observations show that zircon, thorite, columbite-(Mn), and bastnäsite are the dominant primary U-bearing accessory minerals in the Yangzhuang granite porphyry. These accessory minerals mainly occur in the matrix. Zircon mainly appears as isolated subhedral to euhedral crystals and shows a characteristic oscillatory zoning texture (Fig. 4f). Zircon crystals range in size from 10 to 250 μm. Pristine columbite-(Mn) (Fig. 4e) and thorite mainly occur as subhedral to euhedral crystals and display no compositional heterogeneity. The sizes of thorite and columbite-(Mn) crystals can be up to 150 μm and 200 μm, respectively.

Generally, the changes in textures and compositions of U-bearing accessory minerals such as zircon, allanite, and monazite during hydrothermal alteration may be reflected by BSE images (e.g., Cuney and Mathieu 2000; Hecht and Cuney 2000; Poitrasson 2002; Geisler et al. 2003; Nasdala et al. 2009). For instance, the altered domains of zircon usually have lower BSE intensities compared to the unaltered domains (e.g., Geisler et al. 2003; Nasdala et al. 2009). Unaltered and altered zircon, thorite, and columbite-(Mn) varieties have been found in the altered samples of the granite porphyry

(Fig. 5). Petrographic observations show that most of the accessory minerals that occur in the matrix have undergone various degrees of alteration in the altered samples. Relict domains of accessory minerals and their altered areas have sharp contacts. The altered domains of zircon, thorite, and columite-(Mn) show lower BSE intensities than those of the unaltered domains (Figs. 5a-b and 5g-h). Some zircon grains have irregular and partially dissolved grain boundaries (Figs. 5a, 5c, and 5e), which may imply dissolution of zircon. Many micro-cracks are observed in the altered zircon and thorite grains (Figs. 5a and 5g). There are numerous U-Zr-REE silicate-filled microveinlets on grain boundaries or within fissures in the vicinity of altered accessory minerals such as thorite (Fig. 5f) and zircon (Figs. 5d and 5e).

Whole-rock major and trace elements

The whole-rock geochemical data of the Yangzhuang granite porphyry were collected from Mao et al. (2014), Zhang and Zhang (2014), and this study. The Yangzhuang granite porphyry has concentrations of SiO_2 (75.2–78.3 wt%, mean = 76.6 wt%), K_2O + Na_2O (8.5–9.3 wt%), CaO (0.3–1.0 wt%), MgO (0.01–0.12 wt%), F (0.03–0.50 wt%). The granite porphyry shows a meta-aluminous to weakly peraluminous character with A/CNK ranging from 0.93 to 1.08. The granite porphyry has U concentrations ranging from 3.5 to 76.4 ppm (mean = 12.3 ppm) with Th/U ratios (0.37 to 7.11). In addition, the granite porphyry has concentrations of Be (4.2 to 71.7 ppm,

mean = 13.7), Nb (81.9–121.0 ppm, mean = 97.8 ppm), Zr (162.0–215.1 ppm, mean = 192.7 ppm), and Ta (5.7–9.4 ppm). These results indicate that the Yangzhuang granite porphyry may be a good source of U and Be for the formation of the Baiyanghe deposit. The altered samples of the granite porphyry have SiO_2 (74.4–77.6 wt%, mean = 76.3 wt%), K_2O + Na_2O (6.2–10.2 wt%), CaO (0.3–2.6 wt%), MgO (0.07–0.14 wt%), F (0.02–0.04 wt%) (Supplementary Table 2). Compared to the least-altered samples, they have relatively low concentrations of U (2.7–8.7 ppm, mean = 5.0 ppm) and Be (5.0–6.6 ppm, mean = 5.5 ppm).

The Baiyanghe U-Be mineralization is closely associated with the Devonian tuff (Wang et al. 2012; Li et al. 2015). The least-altered tuff has concentrations of SiO_2 (74.5–78.8 wt%), Al_2O_3 (9.8–10.4 wt%), K_2O + Na_2O (6.9–7.1 wt%), CaO (0.8–1.0 wt%), MgO (0.07–0.09 wt%), U (2.21–2.44 ppm), and Be (2.31–2.53 ppm) (Supplementary Table 2). In contrast, the altered sample (BY-1) of tuff has elevated concentrations of Al_2O_3 (12.3 wt%), MgO (0.3 wt%), Be (12.3 ppm), and U (10.2 ppm).

Mineral compositions and (isotope) geochemistry

Mica and feldspars. The major and minor element characteristics of mica in the Yangzhuang granite porphyry obtained by EPMA have been discussed by Zhang et al. (2019). The mica has concentrations of SiO_2 (42.16–46.36 wt%), Al_2O_3 (17.22–20.58

wt%), MnO (6.93–9.32 wt%), and FeO (6.98–9.53 wt%) and may be classified as zinnwaldite (Zhang et al. 2019). The trace element results of the mica are listed in Supplementary Table 5. The mica has concentrations of Be (50–64 ppm), Li (10541–13614 ppm), Nb (134–492 ppm), Rb (2360–3893 ppm), and U (0.28–1.22 ppm). The Be concentration in the mica is nearly five times higher than that of the Yangzhuang granite porphyry (Be_{mean} = 13.7 ppm) and ten times higher than the average concentration of Be (5.4 ppm) in biotite from the Spor Mountain rhyolite (Dailey et al. 2018). In addition, the mica also contains detectable amounts of Sc, Ta, Mo, V, Cr, Cs, La, Ce, Y, and Pb.

Electron probe micro-analyses show that K-feldspars that occur as phenocrysts and in the matrix of the granite porphyry have similar chemical compositions with concentrations of Or (95.12–99.28 mol%) and Ab (0.72–4.87 mol%). Plagioclase that appears as matrix has Or (0.51–1.46 mol%), Ab (98.38–99.45 mol%), and negligible An (0–0.41 mol%).

Zircon. Analyses of the pristine zircon and unaltered domains of zircon grains found in the Yangzhuang granite porphyry have concentrations of ZrO_2 in the range of 59.04–64.16 wt%, SiO_2 of 32.17–34.18 wt%, HfO_2 of 0.74–3.28 wt%, and UO_2 of 0.51–1.43 wt%. The altered domains of zircon grains are characterized by higher concentrations of Y, Fe, Ca, P, F, Al, and Th, but lower concentrations of Zr, Si, and U

relative to the relicts of the primary grains (Supplementary Table 4, Figs. 6 and 7). The altered domains of zircon show considerable increases in Y_2O_3 (3.29–20.03 wt%) and FeO (0.62–17.64 wt%). No other elements were identified during exploratory EDS analysis that may account for the low EPMA totals, and therefore it is concluded that the zircon is hydrated (Geisler et al. 2007). Figure 8 shows that Zr and U have been mobilized along fissures or boundaries of the rock-forming minerals in the vicinity of the altered zircon. The negative correlations of (Al + P) and Si, (REE+Y) and Zr, and (Ca + Fe + Mg) and Zr (Figs. 6a-c) suggest that the incorporation of Ca, Fe, Mg, REE, and Y into the structure of the altered areas is presumably counterbalanced by Zr loss, and the incorporation of Al and P may be explain by the substitution $P^{5+} + Al^{3+} = 2Si^{4+}$ (Hoskin and Schaltegger 2003; Bouvier et al. 2012).

Columbite-(Mn). Columbite-(Mn) is the main host of Nb and Ta in the Yangzhuang granite porphyry with Nb_2O_5 (71.43–76.46 wt%) and MnO (12.97–16.54 wt%) being the dominant constituents. Additionally, significant abundances of Ta_2O_5 (0.82–3.12 wt%), FeO (2.94–6.23 wt%), TiO_2 (1.79–5.88 wt%), UO_2 (0.20–0.88 wt%), and Mo (290–566 ppm) were documented. The altered domains of columbite-(Mn) crystals have higher concentration of Ti but lower Nb concentration than those of the relict domains (Fig. 9). The altered domains are close in composition to rutile (Supplementary Table 4). The altered domains display variable concentrations of Nb_2O_5

(3.92–17.34 wt%), Ta_2O_5 (0.30–1.09 wt%), UO_2 (0–0.26 wt%), and FeO (1.48–14.03 wt%). However, the average concentrations of these elements are lower than those of the unaltered domains. The negative correlation of (Nb_2O_5 + Ta_2O_5 + FeO) and TiO_2 (Fig. 6d) indicates that the incorporation of Ti into the structure of the altered domains is likely counterbalanced by Nb, Ta, and Fe loss.

The pristine columbite-(Mn) grains yielded a lower intercept age of 308 ± 7 Ma and a ^{207}Pb-corrected weighted mean ^{206}Pb/^{238}U age of 310 ± 4 Ma (MSWD = 1.5) obtained from the Tera-Wasserburg diagram (Fig. 10).

Thorite. Pristine crystals and unaltered domains of thorite from the Yangzhuang granite porphyry have ThO_2 abundances in the range of 65.24–77.63 wt%, SiO_2 between 13.29 and 20.48 wt%, and a wide range of UO_2 concentrations (0.53–11.02 wt%). The altered domains have variable concentrations of ThO_2 (20.10–52.92 wt%), FeO (4.42–17.94 wt%), SiO_2 (11.19–39.90 wt%), and UO_2 (0.52–5.40 wt%). The altered domains of thorite grains have much higher average concentrations of Zr, Fe, Ca, Nb, and P but lower Th, U, and REEs than those of the relict domains. EPMA element mapping of a representative metamict thorite grain (Fig. 11) demonstrates that U, Ce, Y, Fe, and Yb have been mobilized along boundaries of quartz and K-feldspar grains.

This is a preprint, the final version is subject to change, of the American Mineralogist (MSA)
Cite as Authors (Year) Title. American Mineralogist, in press.
DOI: https://doi.org/10.2138/am-2020-7383

DISCUSSION

The temporal framework of the Baiyanghe deposit

The new LA-ICP-MS columbite-(Mn) U-Pb age, combined with previous studies (Ma et al. 2010; Zhang and Zhang 2014; Yi 2016; Miao et al. 2018; Xia 2019), help construct a geochronological framework that includes the magmatism and U-Be mineralization in the Baiyanghe deposit (Fig. 12). The columbite-(Mn) samples yielded a weighted mean $^{206}Pb/^{238}U$ age of 310 ± 4 Ma, which overlaps within error of the zircon U-Pb age of 313 ± 2.3 Ma (Zhang and Zhang 2014), suggesting that the Yangzhuang granite porphyry was emplaced during the Late Carboniferous.

Several diabase and diorite dykes intruded the Baiyanghe deposit (Fig. 2a). Their emplacement ages have been investigated in several studies (e.g., Ma et al. 2010; Miao et al. 2019). For example, the diabase dyke in the No. 2 U-Be occurrence has plagioclase Ar-Ar age of 254 ± 1.9 Ma (Ma et al. 2010). The diabase dyke in the No. 3 occurrence has zircon U-Pb age of 272.2 ± 4 Ma (Miao et al. 2019). The diorite dykes in the No. 3 and 9 occurrences have bulk-rock Rb-Sr age of 298 ± 18 Ma and 222 ± 18 Ma, respectively (Ma et al. 2010). In summary, the diabase and diorite dykes in the Baiyanghe deposit were emplaced during the Early Permian to Late Triassic (Fig. 12).

Field observations (Figs. 3a and 3b) indicate that the Baiyanghe U-Be mineralization might have occurred after the emplacement of the Yangzhuang granite porphyry (Zou and Li 2006). Li et al. (2015) argued that U and Be were most likely leached out from the granite porphyry by hydrothermal fluids. Xia (2019) reported the uraninite U-Pb isochron age of 229 ± 26 Ma for the Baiyanghe uranium mineralization. The time gap between the emplacement age of the Yangzhuang granite porphyry and the age of the uranium mineralization is ~85 M.y., indicating that the uranium mineralization is of post-magmatic origin. However, the uranium mineralization (within error) is contemporaneous with the regional magmatism such as the intrusion of diabase and diorite dykes after the emplacement of the Yangzhuang granite porphyry (Fig. 12). Indeed, the intrusion of mafic dykes plays an important role in the formation of many hydrothermal uranium deposits around the world, such as the Xiangshan, Guidong, and Zhuguangshan uranium ore districts in South China (Hu et al. 2008, 2009; Luo et al. 2015; Zhang et al. 2017; Chi et al. 2020), the Margnac and Fanay uranium deposits in France (Leroy 1978), the Bois Noirs-Limouzat uranium vein in France (Cuney 1978), and the unconformity-type uranium deposits in the Athabasca Basin, Canada (Alexandre et al. 2005). Leroy (1978) argued that the intrusion of mafic dykes in the Massif Central, France, might have heated meteoric waters and triggered the circulation of hydrothermal fluids within U-rich rocks and that the uranium was released from the rocks. Hu et al. (2008, 2009) suggested that crustal extension and associated mafic magmatism in South

China could have heated rocks and allowed CO_2 (probably from mantle sources) to complex U and that the uranium was leached from U-rich rocks. Furthermore, Yi (2016) reported Sm-Nd isochron age of 265 ± 33 Ma for fluorite associated with the Baiyanghe beryllium mineralization. Therefore, the formation of the Baiyanghe U-Be mineralization might be associated with this regional magmatism such as the intrusion of diabase and diorite dykes that might have provided thermal energy for fluid circulation (Leroy 1978; Hu et al. 2008; Chi et al. 2020).

Whole-rock chemical mass balance

Whole-rock major and trace element data presented in Supplementary Table 2 and isocon diagrams (Fig. 13) are used to assess the chemical gains and losses in mass transfer during alteration of the granite porphyry and tuff. The detailed treatment of the calculations and the isocon fitting are referred to that in Grant (1986, 2005). Figure 13a shows the significant gain in CaO and loss in F during the alteration of the granite porphyry, while changes in the other major elements (e.g., Al, Mn, Na, and K) are minor. Of the trace elements in the granite porphyry, Be, Ba, Sr, Pb, U, Zr, Mo, Nb, Ta, Cs, and Hf were lost during alteration. The losses of these elements are reflected by changes in the major or accessory mineral textures and compositions. For example, the loss of Be probably relates to the breakdown of feldspars and zinnwaldite, because Be is dispersed as a trace element in the rock-forming minerals, most commonly the micas and sodic

413 plagioclase in most metaluminous to peraluminous igneous rocks (Kovalenko et al. 1977;
414 London1997; Evensen and London 2002). Indeed, mica in the granite porphyry has much
415 higher concentrations of Be (50–64 ppm) than that of the host rocks (Be_{mean} = 13.7 ppm).
416 The depletion of Mo may be caused by the dissolution of columbite-(Mn) and
417 zinnwaldite in the granite porphyry, as these two minerals have concentrations of Mo of
418 290–566 ppm and 2.72–4.46 ppm, respectively. The losses of Nb and Ta may be related
419 to the dissolution of columbite-(Mn). With regard to the Devonian tuff, Fig. 13b shows
420 losses of K_2O, Ba, and Sr and gains of the other elements such as Al_2O_3, Na_2O, Be, U,
421 Mo, and Nb.

422 **The source of uranium**

423 The formation of the Baiyanghe uranium deposit requires the remobilization of
424 uranium after the emplacement of the Yangzhuang granite porphyry. Zircon, thorite,
425 columbite-(Mn), and bastnäsite are major hosts for uranium in the Yangzhuang granite
426 porphyry. Previous studies show that Th- and U-rich silicate phases such as thorite and
427 zircon may become efficient uranium sources during later fluid circulation events when
428 their structures are destroyed as a result of alpha-recoil during U decay (metamictization)
429 (Pagel 1982; Cuney 2014; McGloin et al. 2016). Thorite and zircon in the Yangzhuang
430 granite porphyry formed with high U and/or Th (Supplementary Table 4) and the host
431 minerals could become metamict after ~85 M.y. (Murakami et al. 1991; Meldrum et al.

1998; Palenik et al. 2003; Nasdala et al. 2005). Uranium could subsequently be mobilized and leached during hydrothermal fluid infiltration (Lee and Tromp 1995; Nasdala et al. 2009, 2010; McGloin et al. 2016).

The whole-rock isocon diagram (Fig. 13a) suggests the mobilization of elements such as U, Nb, Zr, Be, and Ta during alteration of the granite porphyry. Low concentrations of Nb, Mn, U, and Ta in the altered domains of columbite-(Mn) crystals, coupled with the lack of other Nb-Ta-Mn-bearing phases in the vicinity of the altered columbite-(Mn) crystals, indicate that these elements have been released from columbite-(Mn) by hydrothermal fluids. The U-Zr-REE silicate-filled microveinlets show localized mobilization of these elements in the granite porphyry (Figs. 5d-f), and the close association of these microveinlets with altered zircon and thorite crystals indicates that the elements were mobilized from those sources. The micro-cracks and grain boundaries may act as the channels for the migration of U, Zr, and REE (Bea 1996; Seydoux-Guillaume et al. 2012; Montel and Giot 2013). The alteration of zircon results in U leaching, as indicated by the EPMA element map (Fig. 7e) and the increase of Th/U ratios (0.26 to 2.43) from the relict domains of zircon grains to the altered domains. EPMA element mapping shows that U, Zr, Y, and REEs have been mobilized along fissures and/or boundaries of the major minerals (Figs. 7-9 and 11), which provides direct evidence for U release from these minerals. The Baiyanghe hydrothermal system was

F-rich (Li et al. 2015; Zhang et al. 2019). The close association of fluorite with the altered zircon grain (Fig. 7g) may imply the interaction between zircon and F-rich fluids. Fluorine may be important for the transport of metals such as Th, U, Zr, Be, and REEs in aqueous fluids (Keppler and Wyllie 1990; Peiffert et al. 1996; Barton and Young 2002; Harlov and Aranovich 2018). Therefore, elements such as U, Zr, and REEs might be released from the U-bearing accessory minerals in the Yangzhuang granite porphyry via a combination of early metamictization and subsequent interaction with the F-rich fluids (McGloin et al. 2016).

The Devonian volcanic rocks have lower concentration of U (0.7–6.2 ppm, Zhang et al. 2019) than that of the Yangzhuang granite porphyry (3.5–76.4 ppm). Weak uranium enrichment associated with their precipitation in micro-fractures cannot be entirely excluded because these samples are located only several meters from the ore bodies (Zhang et al. 2019). Therefore, the concentration of U in the Devonian volcanic rocks may be lower than the values (0.7–6.2 ppm). Indeed, the samples collected from a distance of about one kilometer from the contact zones in the north have relatively low concentration of U (2.21–2.44 ppm) (Samples BY-2 and BY-3, Fig. 2a). In addition, the isocon diagram (Fig. 13b) shows the gain of U in the tuff during alteration. These results suggest that the Devonian volcanic rocks might not contribute uranium to the formation of the Baiyanghe deposit.

Uraninite is the main uranium ore mineral in the Baiyanghe deposit and it has high concentrations of Nb (1.53–3.02 wt%) and Zr (0.23–0.88 wt%) (Zhang et al. 2019). Compared with the Nb concentrations in the Late Silurian-Early Devonian Xiemisitai volcanic rocks (Nb_{mean} = 6.4 ppm, Shen et al. 2012) and in the Early Devonian Baiyanghe volcanic rocks (Nb_{mean} = 19.6 ppm, Zhang et al. 2019), the Yangzhuang granite porphyry with high Nb concentration (Nb_{mean}= 97.8 ppm) is more likely the major source of Nb present in the Baiyanghe uraninite. Element maps (Figs. 7-9) indicate that Zr and Nb have been mobilized during the alteration of zircon and columbite-(Mn). The isocon diagram (Fig. 13a) also suggests the mobilization of Nb and Zr during the alteration of the granite porphyry.

Implications for the source of beryllium

If the model of Zou and Li (2006) and Li et al. (2015) for the formation of the Baiyanghe deposit is correct, only when the ore-forming material (e.g., U and Be) was leached out from the source rocks might the beryllium mineralization occur. The Yangzhuang granite porphyry has much higher Be concentration (4.2 to 71.7 ppm) than that of the tuff (2.31 to 2.53 ppm). Therefore, the Yangzhuang granite porphyry is more likely to be the source of Be in the Baiyanghe deposit. Accessory magmatic Be-bearing minerals such as beryl have not yet been found in the Yangzhuang granite porphyry. The high concentrations of Be (50–64 ppm) in the mica from the Yangzhuang granite

489 porphyry indicate that Be may be mainly hosted in rock-forming minerals such as mica
490 and feldspars (Kovalenko et al. 1977; London 1997; Evensen and London 2002).
491 Therefore, Be may be released during the breakdown of feldspars and mica. The isocon
492 diagrams (Fig. 13) show the loss of Be in the granite porphyry but Be gain in the tuff
493 during alteration, which suggests that the granite porphyry probably represents the major
494 source of Be in the Baiyanghe deposit (Li et al. 2015; Zhang et al. 2019).

495 ## IMPLICATIONS

496 This study provides new insights into ore sources and enrichment processes of
497 post-magmatic hydrothermal uranium deposits. It also provides an example illustrating
498 the application of primary versus altered U-bearing mineral-assemblages and their trace
499 element abundances and textures to trace the source of uranium for uranium deposits that
500 the study of deposit geochemistry and mineralogy may not effectively reveal. The
501 Baiyanghe uranium deposit is an example of post-magmatic hydrothermal uranium
502 deposits. Zircon, thorite, columbite-(Mn), and bastnäsite are the major U-bearing
503 accessory minerals in the Yangzhuang granite porphyry. EPMA element mapping shows
504 that U, Zr, Y, and HREE have been mobilized during the accessory mineral alteration.
505 Whole-rock isocon diagrams suggest U leaching from the granite porphyry during
506 alteration. Consequently, the Yangzhuang granite porphyry represents the primary source
507 of uranium for the formation of the Baiyanghe uranium deposit. Isocon diagrams show

508 the loss of Be during the alteration of the granite porphyry. This study also provides
509 insights into the source of Be in the Baiyanghe deposit.

510 The model presenting evidence for a link between the uranium source and U
511 ore-assemblage in the Baiyanghe deposit may be applied to many types of post-magmatic
512 hydrothermal uranium deposits such as the granite-related, volcanic, and sandstone
513 because their primary sources of uranium are represented by granites and/ or equivalent
514 volcanic rocks (Cuney 2014). The primary sources of uranium for hydrothermal uranium
515 deposits associated with granites are generally magmatic U-rich minerals that are easily
516 leachable (e.g., uraninite) or become metamict (e.g., zircon, thorite, and allanite) (Pagel
517 1982; Cuney and Friedrich 1987; Cuney 2014; McGloin et al. 2016). Consequently,
518 uranium leaching from U-rich minerals in granites is a key step to forming hydrothermal
519 uranium deposits. This study highlights the potential of element mapping in obtaining
520 direct evidence for uranium leaching from source rocks and in tracing the source of
521 uranium in ore deposits.

522 ## ACKNOWLEDGEMENTS

523 We are very grateful to the editor Hongwu Xu and associate editor Callum Hetherington, as well
524 as three anonymous referees for their constructive comments that have significantly improved the
525 manuscript. We also thank to Zhenyu Chen from the Institute of Mineral Resources, Chinese

Academy of Geological Sciences for his help with electron-microprobe data collection. This study was financially supported by the Key Research Program of the Institute of Geology and Geophysics, CAS (Grant No. IGGCAS-201902), the National Natural Science Foundation of China (Grant No. 41972087), and the China National Nuclear Corporation (Grant No. LTD1603). We wish to thank Jeffrey de Fourestier from the Key State Laboratory of Nuclear Resources and Environment, East China University of Technology for polishing this manuscript and his helpful comments.

REFERENCES CITED

Alexandre, P., Kyser, K., Polito, P., and Thomas, D. (2005) Alteration mineralogy and stable isotope geochemistry of Paleoproterozoic basement-hosted unconformity-type uranium deposits in the Athabasca Basin, Canada. Economic Geology, 100, 1547–1563.

Barton, M.D., and Young, S. (2002) Non-pegmatitic deposits of beryllium: mineralogy, geology, phase equilibria and origin. In E.S. Grew, Ed., Beryllium: Mineralogy, Petrology, and Geochemistry, 50, 591–691. Reviews in Mineralogy and Geochemistry, Mineralogical Society of America, Chantilly, Virginia.

Bea, F. (1996) Residence of REE, Y, Th and U in granites and crustal protoliths: implications for the chemistry of crustal melts. Journal of Petrology, 7, 521–552.

Bonnetti, C., Cuney, M., Bourlange, S., Deloule, E., Poujol, M., Liu, X.D., Peng, Y.B., and Yang, J.X. (2017) Primary uranium sources for sedimentary-hosted uranium deposits in NE China: insight from basement igneous rocks of the Erlian Basin. Mineralium Deposita, 52, 297–315.

545 Bouvier, A.S., Ushikubo, T., Kita, N.T., Cavosie, A.J., Kozdon, R., and Valley, J.W. (2012) Li
546 isotopes and trace elements as a petrogenetic tracer in zircon: insights from Archean TTGs and
547 sanukitoids. Contributions to Mineralogy and Petrology, 163, 745–768.
548 Chabiron, A., Cuney, M., and Poty, B. (2003) Possible uranium sources for the largest uranium district
549 associated with volcanism: the Streltsovka caldera (Transbaikalia, Russia). Mineralium Deposita,
550 38, 127–140.
551 Che, X.D., Wu, F.Y., Wang, R.C., Gerdes, A., Ji, W.Q., Zhao, Z.H., Yang, J.H., and Zhu, Z.Y. (2015)
552 In situ U-Pb isotopic dating of columbite–tantalite by LA-ICP-MS. Ore Geology Reviews, 65,
553 979–989.
554 Chen, J.F., Han, B.F., Ji, J.Q., Zhang, L., Xu, Z., He, G. Q., and Wang, T. (2010) Zircon U-Pb ages
555 and tectonic implications of Paleozoic plutons in northern West Junggar, North Xinjiang,
556 China. Lithos, 115, 137–152.
557 Chen, J.F., Han, B.F., Zhang, L., Xu, Z., Liu, J.L., Qu, W.J., Li, C., Yang, J.H., and Yang, Y.H. (2015)
558 Middle Paleozoic initial amalgamation and crustal growth in the West Junggar (NW China):
559 Constraints from geochronology, geochemistry and Sr–Nd–Hf–Os isotopes of calc-alkaline and
560 alkaline intrusions in the Xiemisitai-Saier Mountains. Journal of Asian Earth Sciences, 113,
561 90–109.
562 Chen, J.F., Ma, X., Simon, A., Du, H.Y., Han, B.F., Liu, J.L., and Liu, B. (2019) Late Ordovician to
563 early Silurian calc-alkaline magmatism in the Xiemisitai Mountains, northern West Junggar: a
564 response to the subduction of the Junggar-Balkhash Ocean. International Geology Review, 1–21.

565 Chi, G.X., Ashton, K., Deng, T., Xu, D.R., Li, Z.H., Song, H., Liang, R., and Kennicott, J. (2020)
566 Comparison of granite-related uranium deposits in the Beaverlodge district (Canada) and South
567 China–a common control of mineralization by coupled shallow and deep-seated geologic
568 processes in an extensional setting. Ore Geology Reviews, 117, 103319.
569 Choulet, F., Faure, M., Cluzel, D., Chen, Y., Lin, W., Wang, B., and Jahn, B.M. (2012) Architecture
570 and evolution of accretionary orogens in the Altaids collage: the early Paleozoic West Junggar
571 (NW China). American Journal of Science, 312, 1098–1145.
572 Christiansen, E.H., Kowallis, B.J., Dorais, M.J., Hart, G.L., Mills, C.N., Pickard, M., and Parks, E.
573 (2015) The record of volcanism in the Brushy Basin Member of the Morrison Formation:
574 Implications for the Late Jurassic of western North America. The Geological Society of America
575 Special Paper, 513, 399–439.
576 Cuney, M. (1978) Geologic environment, mineralogy, and fluid inclusions of the Bois Noirs-Limouzat
577 uranium vein, Forez, France. Economic Geology, 73, 1567–1610.
578 Cuney, M. (2009) The extreme diversity of uranium deposits. Mineralium Deposita, 44, 3–9.
579 Cuney, M. (2014) Felsic magmatism and uranium deposits. Bulletin de la Société Géologique de
580 France, 185, 75–92.
581 Cuney, M., and Friedrich, M. (1987) Physicochemical and crystal-chemical controls on accessory
582 mineral paragenesis in granitoids: implications for uranium metallogenesis. Bulletin de
583 mineralogy, 110, 235–247.

584 Cuney, M., and Kyser, K. (2008) Recent and not-so-recent developments in uranium deposits and
585 implications for exploration. Mineralogical Association of Canada, Short Course Series, 39,
586 1–257.
587 Cuney, M., and Mathieu, R. (2000) Extreme light rare earth element mobilization by diagenetic fluids
588 in the geological environment of the Oklo natural reactor zones, Franceville basin,
589 Gabon. Geology, 28, 743–746.
590 Dahlkamp, F.J. (1993) Uranium deposits of the world. Springer, Berlin, Heidelberg, pp. 1–449.
591 Dailey, S.R., Christiansen, E.H., Dorais, M.J., Kowallis, B.J., Fernandez, D.P., and Johnson, D.M.
592 (2018) Origin of the fluorine- and beryllium-rich rhyolites of the Spor Mountain Formation,
593 Western Utah. American Mineralogist, 103, 1228–1252.
594 Evensen, J.M., and London, D. (2002) Experimental silicate mineral/melt partition coefficients for
595 beryllium and the crustal Be cycle from migmatite to pegmatite. Geochimica et Cosmochimica
596 Acta, 66, 2239–2265.
597 Fayek, M., and Shabaga, B. (2011) The BaiYangHe beryllium deposit, NW China. Internal Report, p.
598 1–26.
599 Förster, H.J. (1999) The chemical composition of uraninite in Variscan granites of the Erzgebirge,
600 Germany. Mineralogical Magazine, 62, 239–252.
601 Gäbler, H.E., Melcher, F., Graupner, T., Bahr, A., Sitnikova, M.A., Henjes-Kunst, F., Oberthür, T.,
602 Brätz, H., and Gerdes, A. (2011) Speeding up the analytical workflow for Coltan fingerprinting

603 by an integrated mineral liberation analysis/LA-ICP-MS approach. Geostandards and
604 Geoanalytical Research, 35, 431–448.
605 Geisler, T., Pidgeon, R.T., Kurtz, R., Bronswijk, W.V., and Schleicher, H. (2003) Experimental
606 hydrothermal alteration of partially metamict zircon. American Mineralogist, 88, 1496–1513.
607 Geisler, T., Schaltegger, U., and Tomaschek, F. (2007) Re-equilibration of zircon in aqueous fluids
608 and melts. Elements, 3, 43–50.
609 Grant, J.A. (1986) The isocon diagram–A simple solution to Gresens' equation for metasomatic
610 alteration. Economic geology, 81, 1976–1982.
611 Grant, J.A. (2005) Isocon analysis: A brief review of the method and applications. Physics and
612 Chemistry of the Earth, Parts A/B/C, 30, 997–1004.
613 Griffin, W.L., Powell, W.J., Pearson, N.J., and O'Reilly, S.Y. (2008) GLITTER: data reduction
614 software for laser ablation ICP-MS. In: P. Sylvester, Ed., Laser ablation-ICP-MS in the earth
615 sciences: Current Practices and Outstanding Issues. Mineralogical Association of Canada Short
616 Course, 40, 204–207.308-311
617 Harlov, D.E., and Aranovich, L. (2018) The role of halogens in terrestrial and extraterrestrial
618 geochemical processes: surface, crust, and mantle. In D.E. Harlov, and L. Aranovich, Eds., The
619 Role of Halogens in Terrestrial and Extraterrestrial Geochemical Processes: surface, crust, and
620 mantle, p. 1–19. Springer Geochemistry, Springer, Cham.

621 Hecht, L., and Cuney, M. (2000) Hydrothermal alteration of monazite in the Precambrian crystalline
622 basement of the Athabasca Basin (Saskatchewan, Canada): implications for the formation of
623 unconformity-related uranium deposits. Mineralium Deposita, 35, 791–795.
624 Hoskin, P.W.O., and Schaltegger, U. (2003) The composition of zircon and igneous and metamorphic
625 petrogenesis. In: J.M. Hanchar, and P.W.O. Hoskin, Eds., Zircon, 53, p. 27–62. Reviews in
626 Mineralogy and Geochemistry, Mineralogical Society of America, Chantilly, Virginia.
627 Hu, R.Z., Bi, X.W., Zhou, M.F., Peng, J.T., Su, W.C., Liu, S., and Qi, H.W. (2008) Uranium
628 metallogenesis in South China and its relationship to crustal extension during the Cretaceous to
629 Tertiary. Economic Geology, 103, 583–598.
630 Hu, R.Z., Burnard, P.G., Bi, X.W., Zhou, M.F., Peng, J.T., Su, W.C., and Zhao, J.H. (2009)
631 Mantle-derived gaseous components in ore-forming fluids of the Xiangshan uranium deposit,
632 Jiangxi province, China: evidence from He, Ar and C isotopes. Chemical Geology, 266, 86–95.
633 Keppler, H., and Wyllie, P.J. (1990) Role of fluids in transport and fractionation of uranium and
634 thorium in magmatic processes. Nature, 348, 531–533.
635 Kovalenko, V.I., Antipin, V.S., and Petrov, L.L. (1977) Distribution coefficients of Be in ongonites
636 and some notes on its behavior in the rare metal lithium-fluorine granites. Geochemistry
637 International, 14, 129–141.
638 Lee, J.K.W., and Tromp, J. (1995) Self-induced fracture generation in zircon. Journal of Geophysical
639 Research: Solid Earth, 100, 17753–17770.

640 Leroy, J. (1978) The Margnac and Fanay uranium deposits of the La Crouzille district (Western
641 Massif Central, France): Geological and fluid inclusion studies. Economic Geology, 73,
642 1611–1634.
643 Li, X.F., Wang, G., Mao, W., Wang, C.Z., Xiao, R., and Wang, M. (2015) Fluid inclusions, muscovite
644 Ar-Ar age, and fluorite trace elements at the Baiyanghe volcanic Be-U-Mo deposit, Xinjiang,
645 northwest China: Implication for its genesis. Ore Geology Reviews, 64, 387–399.
646 London, D. (1997) Estimating abundances of volatile and other mobile components in evolved silicic
647 melts through mineral–melt equilibria. Journal of Petrology, 38, 1691–1706.
648 Luo, J.C., Hu, R.Z., Fayek, M., Li, C.S., Bi, X.W., Abdu, Y., and Chen, Y.W. (2015). In-situ SIMS
649 uraninite U–Pb dating and genesis of the Xianshi granite-hosted uranium deposit, South China.
650 Ore Geology Reviews, 65, 968–978.
651 Ma, H.F., Yi, L.S., Xiu, and X.Q. (2010) Research on evaluation of uranium and beryllium resource
652 potential in Xuemisitan area, Xinjiang Uygur Autonomous Region. Beijing Research Institute of
653 Uranium Geology Internal Report, p. 161 (in Chinese with English abstract).
654 Mao, W., Wang, G., Li, X.F., Wang, M., and Xiao, R. A study of fluid inclusions in Baiyanghe U-Be
655 deposit, Xinjiang. Mineral Deposits, 32, 1026–1034 (in Chinese with English abstract).
656 Mao, W., Li, X.F., Wang, G., Xiao, R., Wang, M., Li, Y.L., Ren, M.C., Bai, Y.P., and Yang, F. (2014)
657 Petrogenesis of the Yangzhuang Nb- and Ta-rich A-type granite porphyry in West Junggar,
658 Xinjiang, China. Lithos, 198, 172–183.

659 Mathieu, R., Zetterström, L., Cuney, M., Gauthier-Lafaye, F., and Hidaka, H. (2001) Alteration of
660 monazite and zircon and lead migration as geochemical tracers of fluid paleocirculations around
661 the Oklo-Okélobondo and Bangombé natural nuclear reaction zones (Franceville basin,
662 Gabon). Chemical Geology, 171, 147–171.
663 McGloin, M.V., Tomkins, A.G., Webb, G.P., Spiers, K., MacRae, C.M., Paterson, D., and Ryan, C.G.
664 (2016) Release of uranium from highly radiogenic zircon through metamictization: The source of
665 orogenic uranium ores. Geology, 44, 15–18.
666 Meldrum, A., Boatner, L.A., Weber, W. J., and Ewing, R.C. (1998) Radiation damage in zircon and
667 monazite. Geochimica et Cosmochimica Acta, 62, 2509–2520.
668 Miao, X.Q., Zhang, X., Zhang, H., Wang, J.R., Liu, Z., Li, C.Z., Shi, Q., Li, W.R., Huang, Y.S., and
669 Ma, Q.Z. (2019) Geochronological and geochemical studies of the OIB-type Baiyanghe dolerites:
670 implications for the existence of a mantle plume in northern West Junggar (NW China).
671 Geological Magazine, 156, 702–724.
672 Montel, J.M., and Giot, R., (2013) Fracturing around radioactive minerals: elastic model and
673 applications. Physics and Chemistry of Minerals, 40, 635–645.
674 Murakami, T., Chakoumakos, B.C., Ewing, R.C., Lumpkin, G.R., and Weber, W.J. (1991)
675 Alpha-decay event damage in zircon. American Mineralogist, 76, 1510–1532.
676 Nasdala, L., Hanchar, J.M., Kronz, A., and Whitehouse, M.J. (2005) Long-term stability of alpha
677 particle damage in natural zircon. Chemical Geology, 220, 83–103.

678 Nasdala, L., Hanchar, J.M., Rhede, D., Kennedy, A. K., and Váczi, T. (2010) Retention of uranium in
679 complexly altered zircon: An example from Bancroft, Ontario. Chemical Geology, 269,
680 290–300.
681 Nasdala, L., Kronz, A., Wirth, R., Váczi, T., Pérez-Soba, C., Willner, A., and Kennedy, A.K. (2009)
682 The phenomenon of deficient electron microprobe totals in radiation-damaged and altered
683 zircon. Geochimica et Cosmochimica Acta, 73, 1637–1650.
684 Nash, J.T. (2010) Volcanogenic uranium deposits: Geology, geochemical processes, and criteria for
685 resource assessment. U.S. Geological Survey, Open-File Report 2010-1001, p. 1–99.
686 Pagel, M. (1982) The mineralogy and geochemistry of uranium, thorium, and rare-earth elements in
687 two radioactive granites of the Vosges, France. Mineralogical Magazine, 46, 149–161.
688 Palenik, C.S., Nasdala, L., and Ewing, R.C. (2003) Radiation damage in zircon. American
689 Mineralogist, 88, 770–781.
690 Peiffert, C.H., Nguyen-Trung, C.H., and Cuney, M. (1996) Uranium in granitic magmas. Part II:
691 experimental determination of uranium solubility and fluid-melt partition coefficients in the
692 UO_2–haplogranite–H_2O–halides systems at 720–770 °C 200 MPa. Geochimica et Cosmochimica
693 Acta, 60, 1515–1529.
694 Poitrasson, F. (2002) In situ investigations of allanite hydrothermal alteration: examples from
695 calc-alkaline and anorogenic granites of Corsica (southeast France). Contributions to Mineralogy
696 and Petrology, 143, 131–132.

697 Seydoux-Guillaume, A.M., Bingen, B., Paquette, J.L., and Bosse, V. (2015) Nanoscale evidence for
698 uranium mobility in zircon and the discordance of U–Pb chronometers. Earth and Planetary
699 Science Letters, 409, 43–48.
700 Seydoux-Guillaume, A.M., Montel, J.M., Bingen, B., Bosse, V., De Parseval, P., Paquette, J.L., Janots,
701 E., and Wirth, R. (2012) Low-temperature alteration of monazite: Fluid mediated coupled
702 dissolution–precipitation, irradiation damage, and disturbance of the U–Pb and Th–Pb
703 chronometers. Chemical Geology, 330, 140–158.
704 Shen, P., Shen, Y.C., Li, X.H., Pan, H.D., Zhu, H.P., Meng, L., and Dai, H.W. (2012) Northwestern
705 Junggar Basin, Xiemisitai Mountains, China: a geochemical and geochronological
706 approach. Lithos, 140, 103–118.
707 Shen, P., Pan, H.D., Cao, C., Zhong, S.H., and Li, C.H. (2017) The formation of the Suyunhe large
708 porphyry Mo deposit in the West Junggar terrain, NW China: Zircon U-Pb age, geochemistry and
709 Sr-Nd-Hf isotopic results. Ore Geology Reviews, 81, 808–828.
710 Tartèse, R., Boulvais, P., Poujol, M., Gloaguen, E., and Cuney, M. (2013) Uranium mobilization from
711 the Variscan Questembert syntectonic granite during fluid-rock interaction at depth. Economic
712 Geology, 108, 379–386.
713 Wang, M., Li, X.F., Wang, G., Li, Y.L., Shi, Z.L., and Lu, K.G. (2012) Geological characteristics of
714 Baiyanghe beryllium-uranium deposits in Xuemisitan volcanic belt, Xinjiang. Mineral
715 Exploration, 3, 34–40 (in Chinese with English abstract).

716 Windley, B.F., Alexeiev, D., Xiao, W., Kro¨ er, A., and Badarch, G. (2007) Tectonic models for
717 accretion of the Central Asian Orogenic Belt. Journal of the Geological Society, 164, 31–47.
718 Xia, Y.L. (2019) Geochronology of uranium mineralization in China, 301 p. China Atomic Energy
719 Press, Beijing (in Chinese).
720 Xiao, W.J., Han, C.M., Yuan, C., Sun, M., Lin, S.F., Chen, H.L., Li, Z.L., and Sun, S. (2008) Middle
721 Cambrian to Permian subduction-related accretionary orogenesis of Northern Xinjiang, NW
722 China: implications for the tectonic evolution of central Asia. Journal of Asian Earth Sciences, 32,
723 102–117.
724 Xie, L.W., Zhang, Y.B., Zhang, H.H., Sun, J.F., and Wu, F.Y. (2008) In situ simultaneous
725 determination of trace elements, U-Pb and Lu-Hf isotopes in zircon and baddeleyite. Chinese
726 Science Bulletin, 53, 1565–1573
727 Xu, Q.J., Liu, S.F., Ye, F.W., Zhang, Z.X., and Zhang, C. (2018) Application of CASI/SASI and
728 fieldspec4 hyperspectral data in exploration of the Baiyanghe uranium deposit, Hebukesaier,
729 Xinjiang, NW China. International Journal of Remote Sensing, 39, 453–469.
730 Xu, Z., Han, B.F., Ren, R., Zhou, Y.Z., Zhang, L., Chen, J.F., Li, S., Li, X.H., and Liu, D.Y. (2012)
731 Ultramafic–mafic mélange, island arc and post-collisional intrusions in the Mayile Mountain,
732 West Junggar, China: implications for Paleozoic intra-oceanic subduction–accretion process.
733 Lithos, 132, 141–161.

734 Yang, G.X., Li, Y.J., Xiao, W.J., Sun, Y., and Tong, L.L. (2014) Petrogenesis and tectonic
735 implications of the middle Silurian volcanic rocks in northern West Junggar, NW
736 China. International Geology Review, 56, 869–884.
737 Yi, L.S. (2016) Geological and geological characteristics, as well as the temporal-spatial evolution of
738 Baiyanghe beryllium-uranium deposit, Xinjiang, 136 p. Ph.D. thesis, University of Chinese
739 Academy of Sciences, Beijing (in Chinese with English abstract).
740 Yin, J.Y., Chen, W., Xiao, W.J., Yuan, C., Windley, B.F., Yu, S., and Cai, K.D. (2017) Late
741 Silurian-early Devonian adakitic granodiorite, A-type and I-type granites in NW Junggar, NW
742 China: Partial melting of mafic lower crust and implications for slab roll-back. Gondwana
743 Research, 43, 55–73.
744 Yin, J.Y., Chen, W., Xiao, W.J., Yuan, C., Sun, M., and Cai, K.D. (2018) Petrogenesis and tectonic
745 implications of early Devonian mafic dike–granite association in the northern West Junggar, NW
746 China. International Geology Review, 60, 87–100.
747 Zhang, L., Chen, Z.Y., Li, S.R., Santosh, M., Huang, G.L., and Tian, Z.J. (2017) Isotope
748 geochronology, geochemistry, and mineral chemistry of the U-bearing and barren granites from
749 the Zhuguangshan complex, South China: Implications for petrogenesis and uranium
750 mineralization. Ore Geology Reviews, 91, 1040–1065.
751 Zhang, L., Li, X.F., Wang, G., Wang, M., Yang, W.L., Zhang, L., and Zhu, Y.T. (2019) Hydrothermal
752 alteration and mineral chemistry of the giant Baiyanghe Be-U deposit in Xinjiang, Northwest
753 China: Implications for its mineralization. Ore Geology Reviews, 111, 102972.

754 Zhang, X., and Zhang, H. (2014) Geochronological, geochemical, and Sr-Nd-Hf isotopic studies of
755 the Baiyanghe A-type granite porphyry in the Western Junggar: Implications for its petrogenesis
756 and tectonic setting. Gondwana Research, 25, 1554–1569.
757 Zou, T.R., and Li, Q.C. (2006) The rare metal and rare metal deposits in Xinjiang, China, 284 p.
758 Geological Publishing House, Beijing (in Chinese).
759

760 # Figure captions

761 **Figure 1.** Simplified geological map of the West Juggar, NW China (modified after Xu et
762 al. 2012; Shen et al. 2017; Zhang et al. 2019).
763 **Figure 2.** (**a**) Geological map of the Baiyanghe deposit (modified after Wang et al. 2012;
764 Li et al. 2015; Zhang et al. 2019). (**b**) Cross-section of the Baiyanghe deposit
765 showing the uranium-beryllium mineralization (modified after Li et al. 2015; Zhang
766 et al. 2019).
767 **Figure 3.** Field images and photomicrographs of the Baiyanghe deposit. (**a**) The contact
768 zones associated with the U-Be mineralization between the granite porphyry and
769 basement. There is abundant purple fluorite at this site. (**b**) The fracture zones within
770 the granite porphyry have purple fluorite. Uraninite (**c**) and bertrandite (**d**)
771 associated with purple fluorite in the ore. Abbreviations: Be = bertrandite, Fl =
772 fluorite, Kfs = K-feldspar, Urn = uraninite, Qz = quartz.

773 **Figure 4.** Microscopic photographs of the least-altered and altered granite porphyry and
774 tuff in the Baiyanghe deposit. (**a** and **b**) Mineral assemblage of quartz, K-feldspar,
775 plagioclase, and zinnwaldite and porphyritic texture of the least-altered granite
776 porphyry (Sample ZK7702-1), Figures a and b were obtained under cross polarized
777 light and by BSE imaging, respectively. (**c** and **d**) The argillization and albitization
778 of K-feldspar phenocryst from the altered sample (No. BYP1-19) of the granite
779 porphyry, Figures c and d were obtained under plane polarized light and by BSE
780 imaging, respectively. Columbite-(Mn) (**e**), zircon (**f**), and bastnäsite (**g**) in the
781 least-altered granite porphyry, BSE images. (**h**) Mineral assemblage and texture of
782 the least-altered tuff (Sample BY-2), under plane polarized light. (**i**) Chlorite and
783 purple fluorite in the altered tuff (Sample BY-1), under plane polarized light.
784 Mineral abbreviations: Ab = albite, Chl = chlorite, Fl = fluorite, Kfs = K-feldspar,
785 Mag = magnetite, Qz = quartz, Znw = zinnwaldite, Zrn = zircon.

786 **Figure 5.** Back-scattered electron images of altered U-bearing accessory minerals in the
787 altered samples of the Yangzhuang granite porphyry. (**a**-**e**) Altered zircons; (**a**) and
788 (**b**) The altered domains are characterized by lower BSE intensities with respective
789 to the relict domains; (**c**) The zircon crystal shows irregular and partially dissolved
790 grain boundaries; (**d**-**e**) Veinlets of the U-Zr-REE silicates along the boundaries of
791 quartz and K-feldspar grains or within fissures in the vicinity of the altered zircon. (**f**)
792 BSE image showing numerous veinlets of the U-Zr-REE silicates along the

boundaries of quartz and K-feldspar grains in the vicinity of the metamict thorite. (**g**) Altered thorite, the altered domains at grain margins have relatively low BSE intensity. (**h**) The altered areas of columbite-(Mn) are marked by relatively low BSE intensity. Mineral abbreviations: Fl = fluorite, Ilt = illite, Kfs = K-feldspar, Mag = magnetite, Qz = quartz, Rt = rutile.

Figure 6. Plots illustrating the substitution mechanism for zircon (on the basis of four oxygen atoms) (**a-c**) and columbite-(Mn) (**d**) in the granite porphyry. (**a**) (Al + P) versus Si. (**b**) (REE + Y) versus Zr. (**c**) (Ca + Fe + Mg) versus Zr. (**d**) TiO_2 versus (Nb_2O_5 + Ta_2O_5 + FeO).

Figure 7. EPMA element maps of an altered zircon grain showing that the altered areas have lower concentrations of Zr, U, and Si, but higher concentrations of Y, Fe, and P relative to the relict areas. Mineral abbreviations: Fl = fluorite, Qz = quartz.

Figure 8. EPMA element maps of an altered zircon grain showing Zr, Ca, and U mobilization. Mineral abbreviations: Ilt = illite, Qz = quartz.

Figure 9. EPMA element maps of a partly altered columbite-(Mn) grain showing that the altered areas have higher concentrations of Ti and Fe, but lower concentration of Nb relative to the unaltered areas. Mineral abbreviations: Kfs = K-feldspar, Qz = quartz.

Figure 10. LA-ICP-MS U-Pb Tera-Wasserburg concordia plot of columbite-(Mn) from the granite porphyry.

812 **Figure 11.** EPMA element maps of a metamict thorite grain showing U, Ce, Yb, and Y
813 mobilization. Mineral abbreviations: Kfs = K-feldspar, Qz = quartz.
814 **Figure 12.** The geochronological framework that includes the magmatism and U-Be
815 mineralization in the Baiyanghe deposit. The data are from: Ma et al. 2010, Zhang
816 and Zhang 2014, Yi 2016; Miao et al. 2019, Xia 2019, This study.
817 **Figure 13** Isocon diagrams for the original and altered granite porphyry (**a**) and tuff (**b**).
818 Major elements are in weight percent oxide, trace elements in ppm. Black lines
819 (isocons) are defined by the constant ratios of element SiO_2, which was used for the
820 calculation of the gains and losses. The whole-rock major and trace element data of
821 the least-altered and altered samples of granite porphyry and tuff are from Mao et al.
822 (2014), Zhang and Zhang (2014), Zhang et al. (2019), and this study.
823

824 ## Supplementary Table captions

825 Table 1 Descriptions and locations of analyzed samples from the Baiyanghe deposit.
826 Table 2 Major and trace elements of the least-altered and altered granite porphyry and
827 tuff from the Baiyanghe deposit.
828 Table 3 EPMA chemical compositions (wt%) of feldspars from the Yangzhuang granite
829 porphyry.

Table 4 EPMA chemical compositions (wt%) of zircon, thorite, and columbite-(Mn) from the Yangzhuang granite porphyry.

Table 5 LA-ICP-MS elemental compositions (ppm) of mica from the Yangzhuang granite porphyry.

Table 6 LA-ICP-MS elemental compositions (ppm) of columbite-(Mn) from the Yangzhuang granite porphyry.

Table 7 LA-ICP-MS U-Pb isotopic ratios and ages for columbite-(Mn) from the Yangzhuang granite porphyry and the Coltan 139.

This is a preprint, the final version is subject to change, of the American Mineralogist (MSA)
Cite as Authors (Year) Title. American Mineralogist, in press.
DOI: https://doi.org/10.2138/am-2020-7383

Figure 1

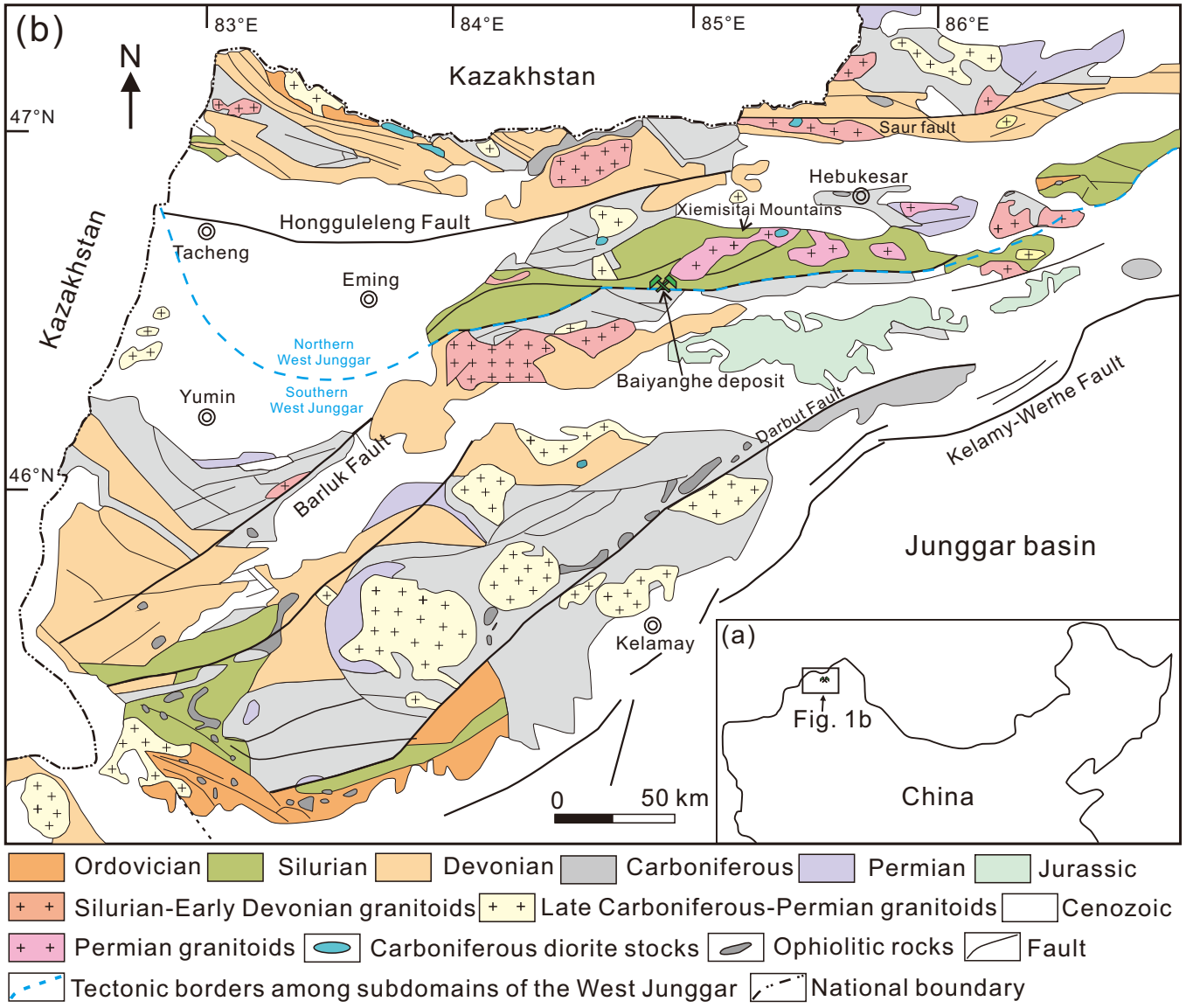

This is a preprint, the final version is subject to change, of the American Mineralogist (MSA)
Cite as Authors (Year) Title. American Mineralogist, in press.
DOI: https://doi.org/10.2138/am-2020-7383

Figure 2

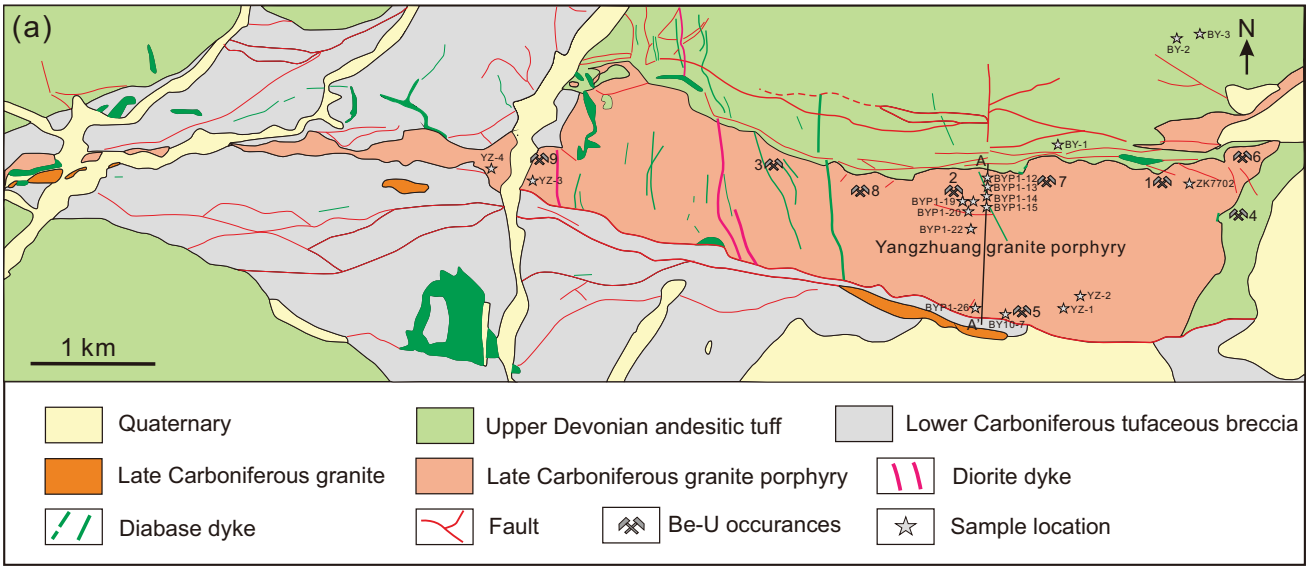

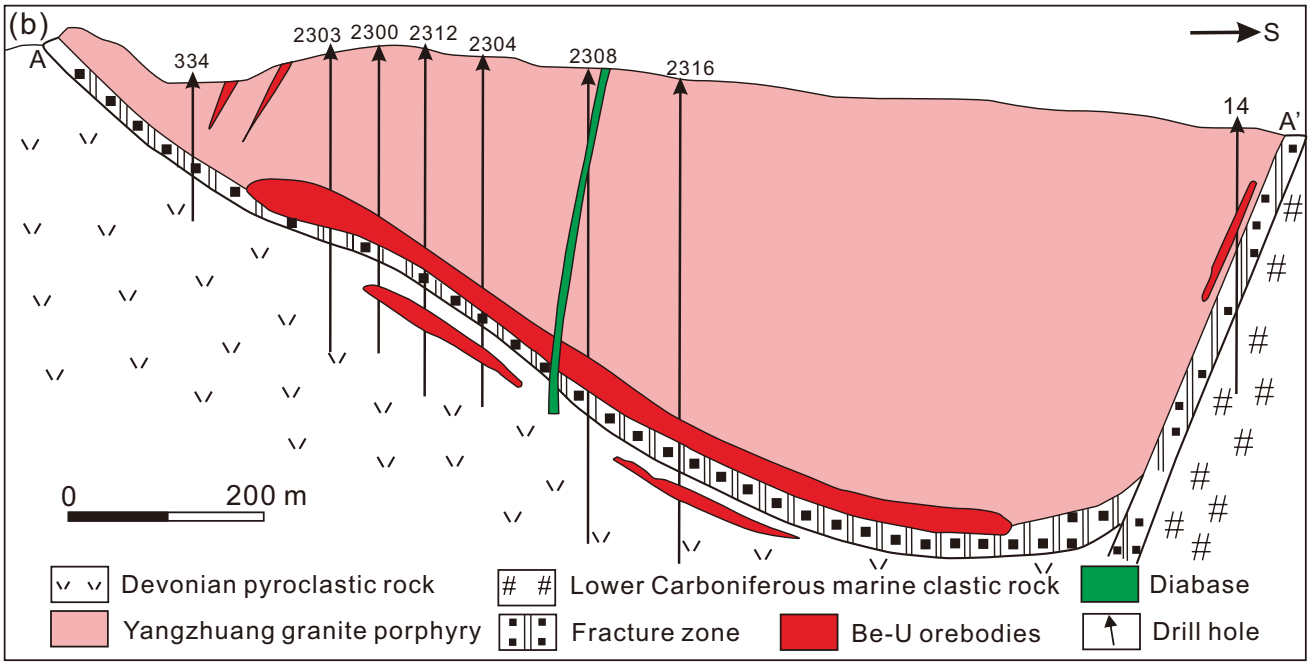

This is a preprint, the final version is subject to change, of the American Mineralogist (MSA)
Cite as Authors (Year) Title. American Mineralogist, in press.
DOI: https://doi.org/10.2138/am-2020-7383

Figure 3

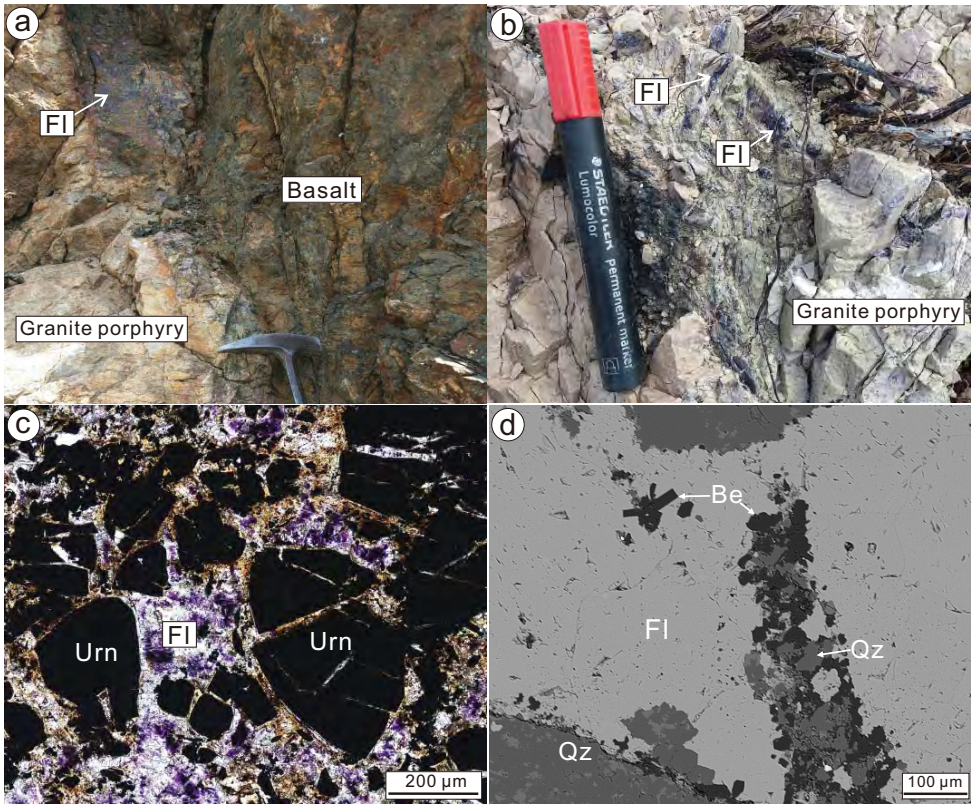

This is a preprint, the final version is subject to change, of the American Mineralogist (MSA)
Cite as Authors (Year) Title. American Mineralogist, in press.
DOI: https://doi.org/10.2138/am-2020-7383

Figure 4

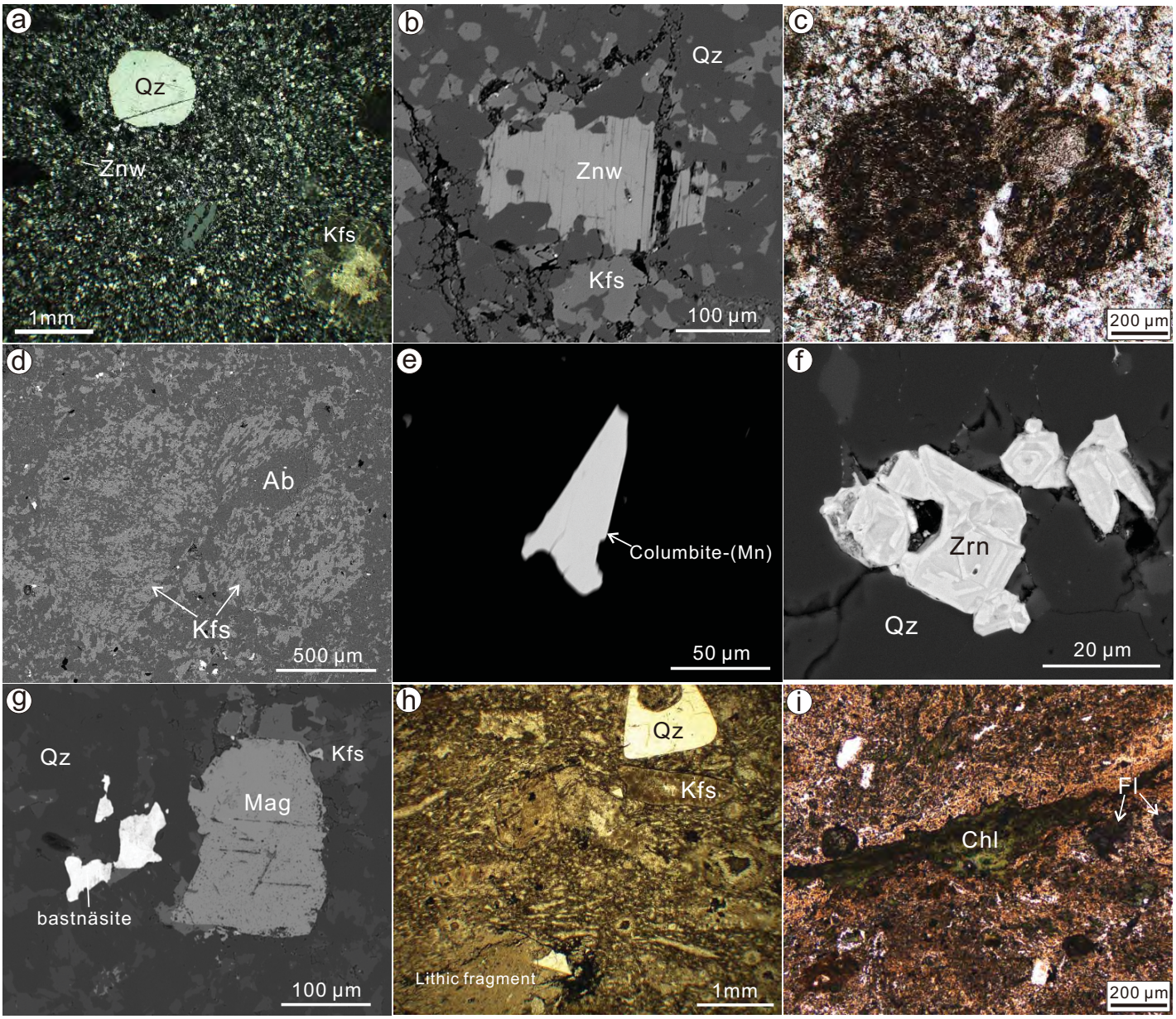

This is a preprint, the final version is subject to change, of the American Mineralogist (MSA)
Cite as Authors (Year) Title. American Mineralogist, in press.
DOI: https://doi.org/10.2138/am-2020-7383

Figure 5

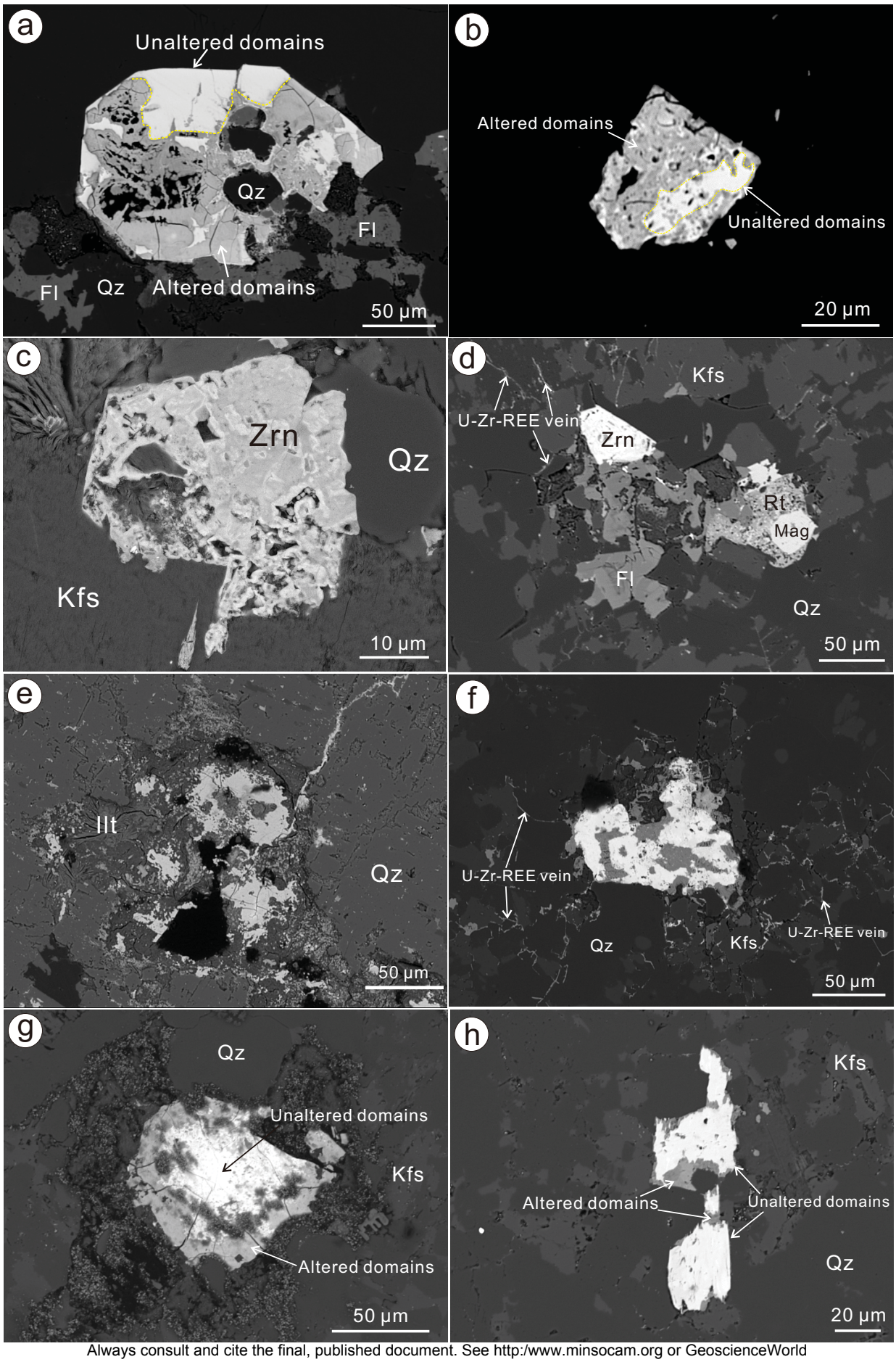

This is a preprint, the final version is subject to change, of the American Mineralogist (MSA)
Cite as Authors (Year) Title. American Mineralogist, in press.
DOI: https://doi.org/10.2138/am-2020-7383

Figure 6

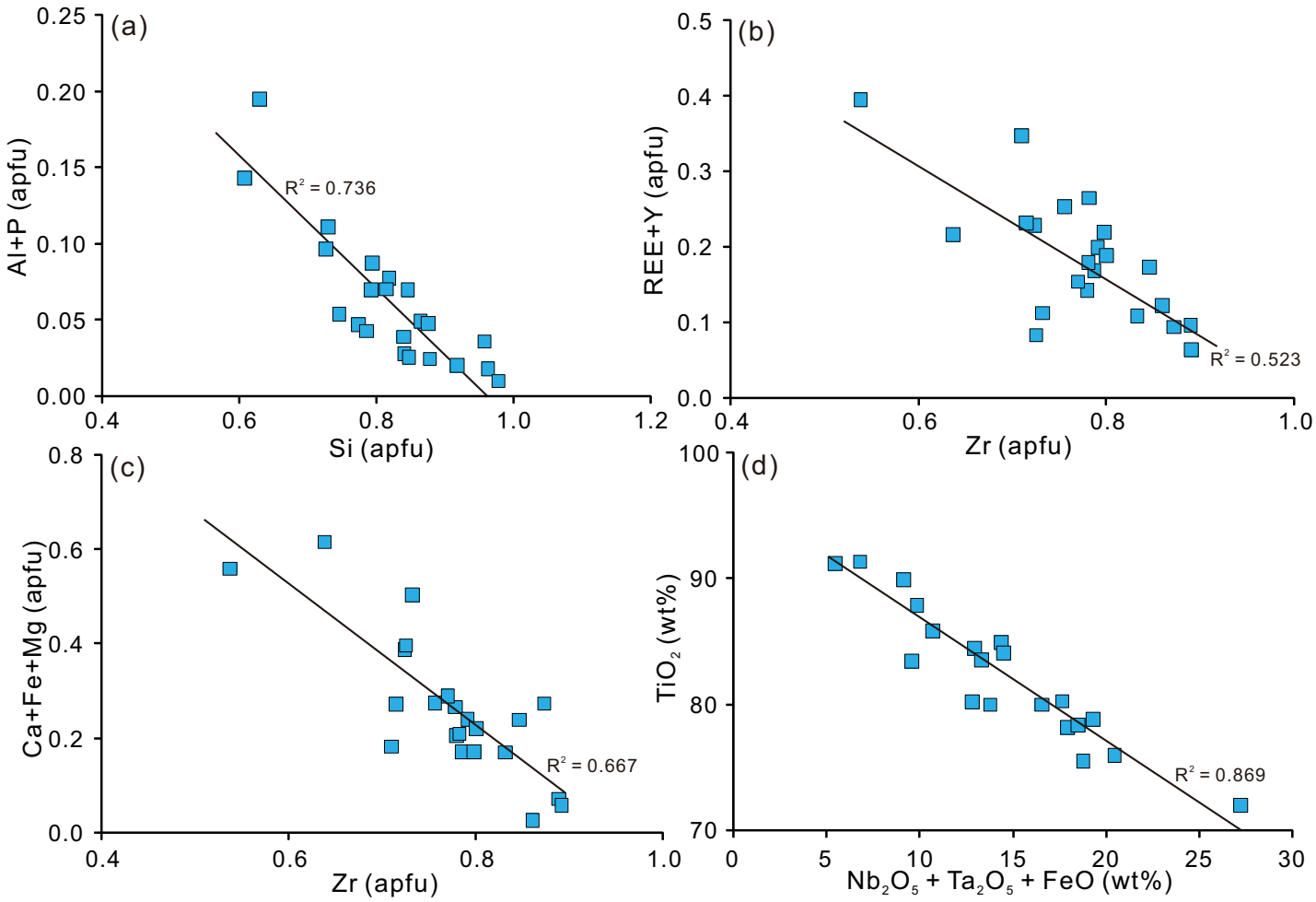

This is a preprint, the final version is subject to change, of the American Mineralogist (MSA)
Cite as Authors (Year) Title. American Mineralogist, in press.
DOI: https://doi.org/10.2138/am-2020-7383

Figure 7

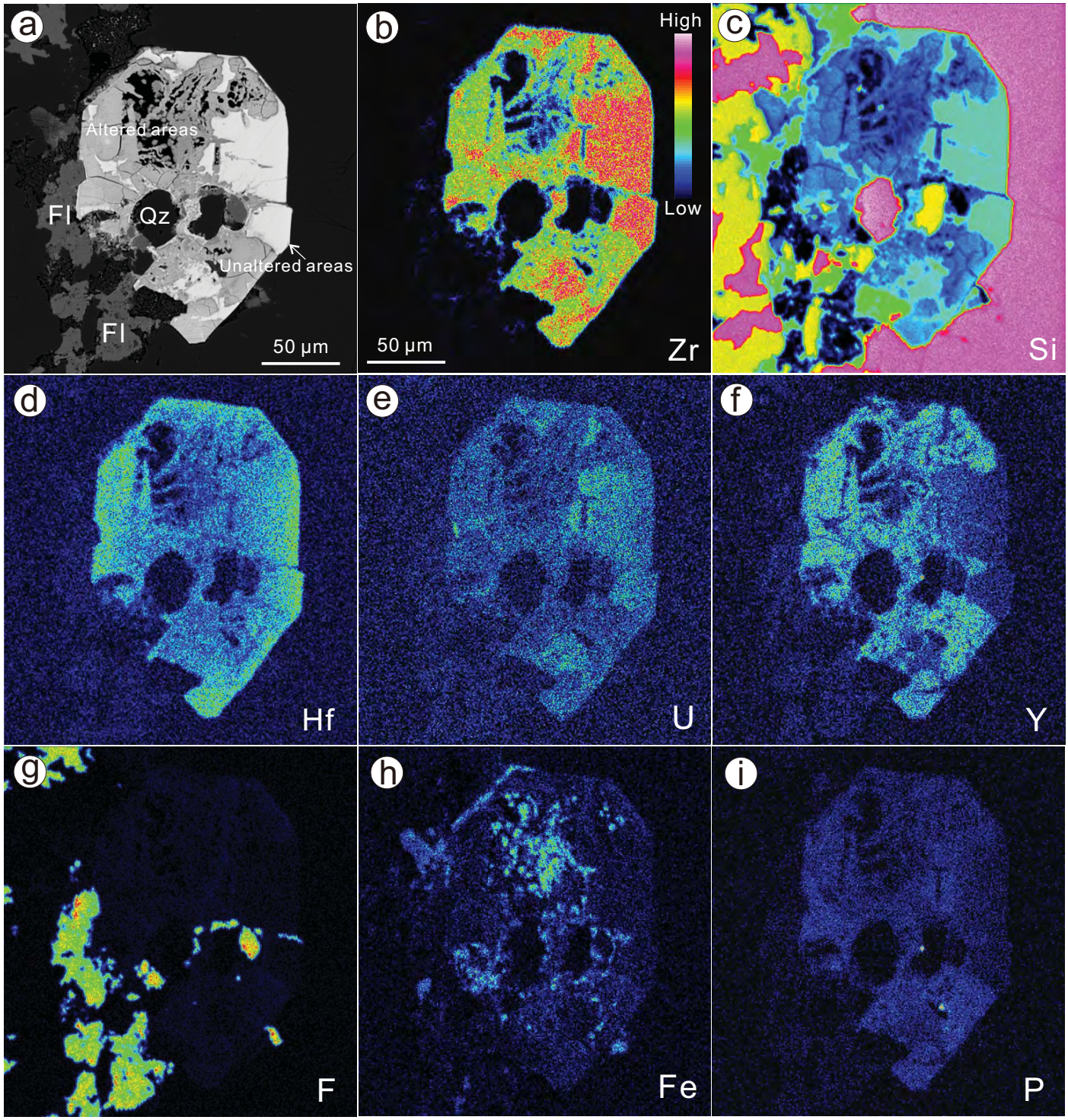

This is a preprint, the final version is subject to change, of the American Mineralogist (MSA)
Cite as Authors (Year) Title. American Mineralogist, in press.
DOI: https://doi.org/10.2138/am-2020-7383

Figure 8

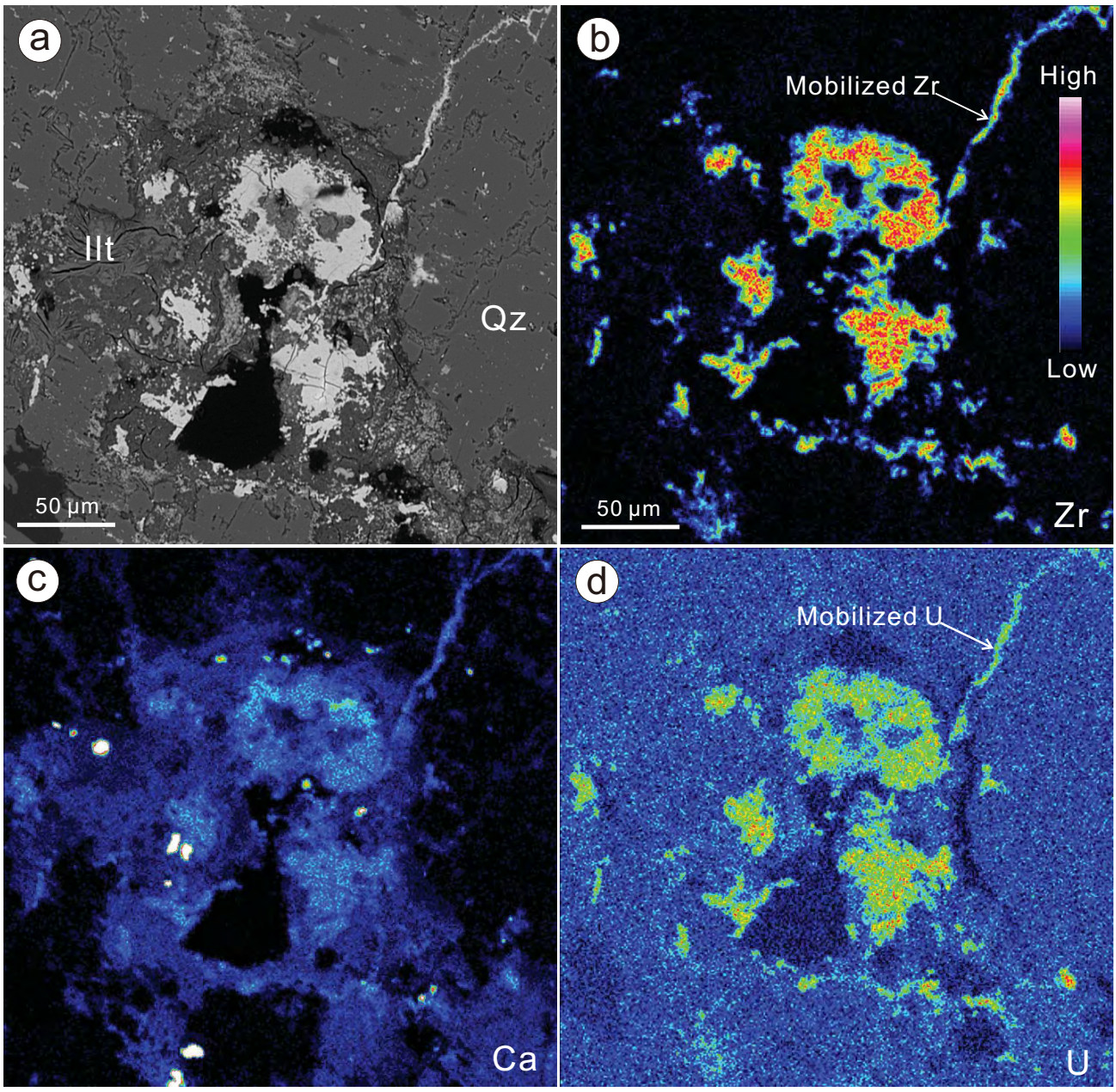

This is a preprint, the final version is subject to change, of the American Mineralogist (MSA)
Cite as Authors (Year) Title. American Mineralogist, in press.
DOI: https://doi.org/10.2138/am-2020-7383

Figure 9

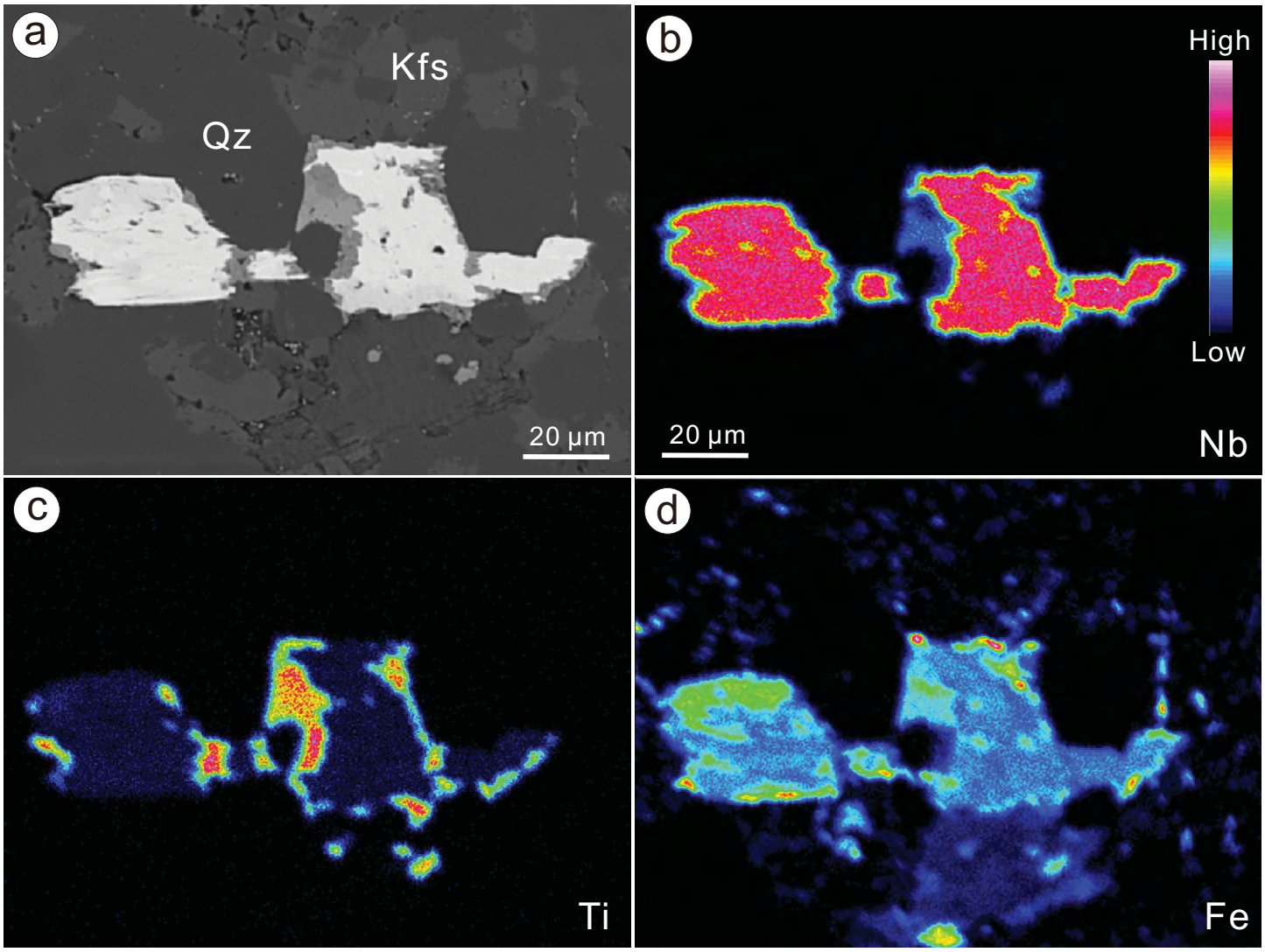

This is a preprint, the final version is subject to change, of the American Mineralogist (MSA)
Cite as Authors (Year) Title. American Mineralogist, in press.
DOI: https://doi.org/10.2138/am-2020-7383

Figure 10

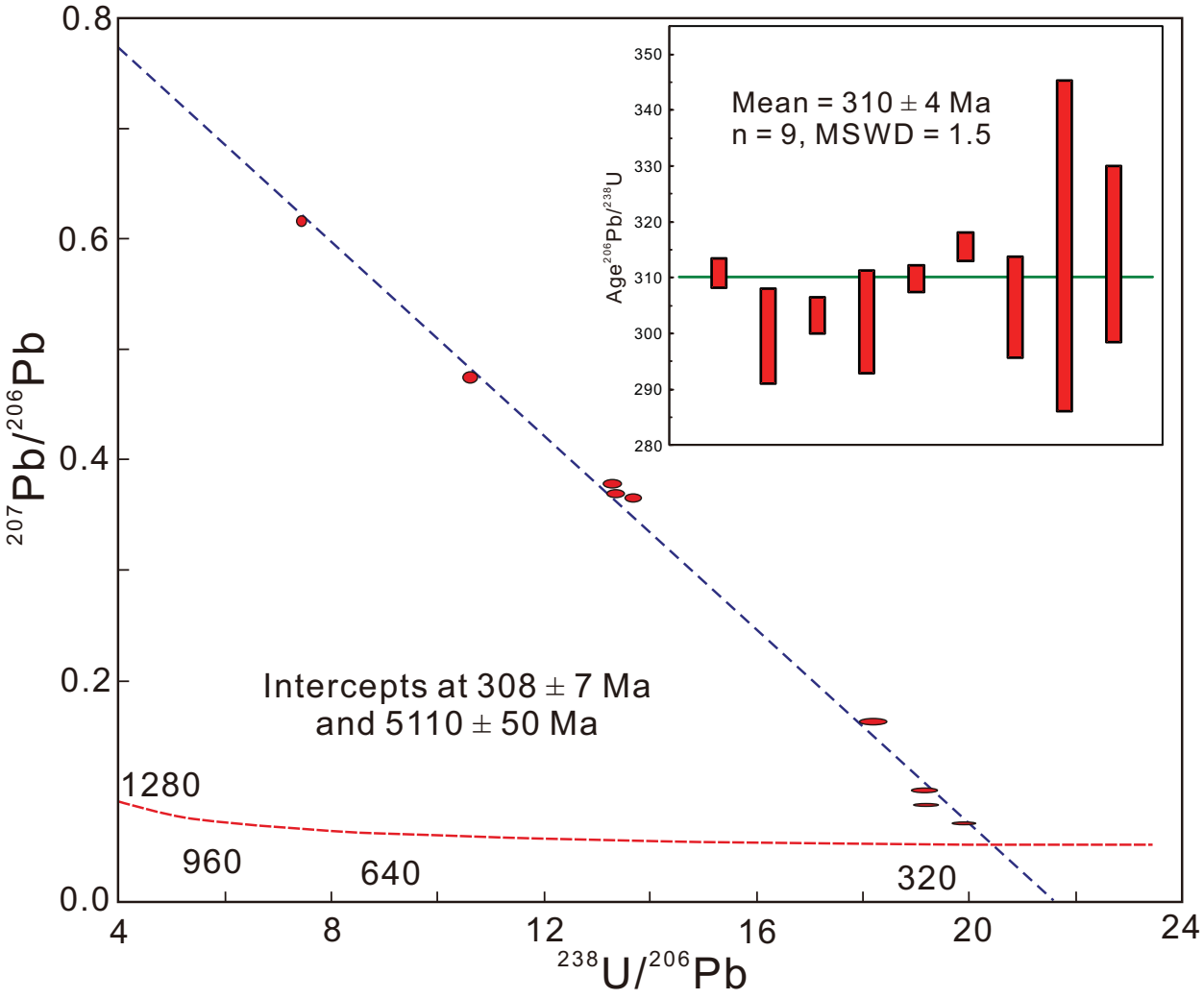

This is a preprint, the final version is subject to change, of the American Mineralogist (MSA)
Cite as Authors (Year) Title. American Mineralogist, in press.
DOI: https://doi.org/10.2138/am-2020-7383

Figure 11

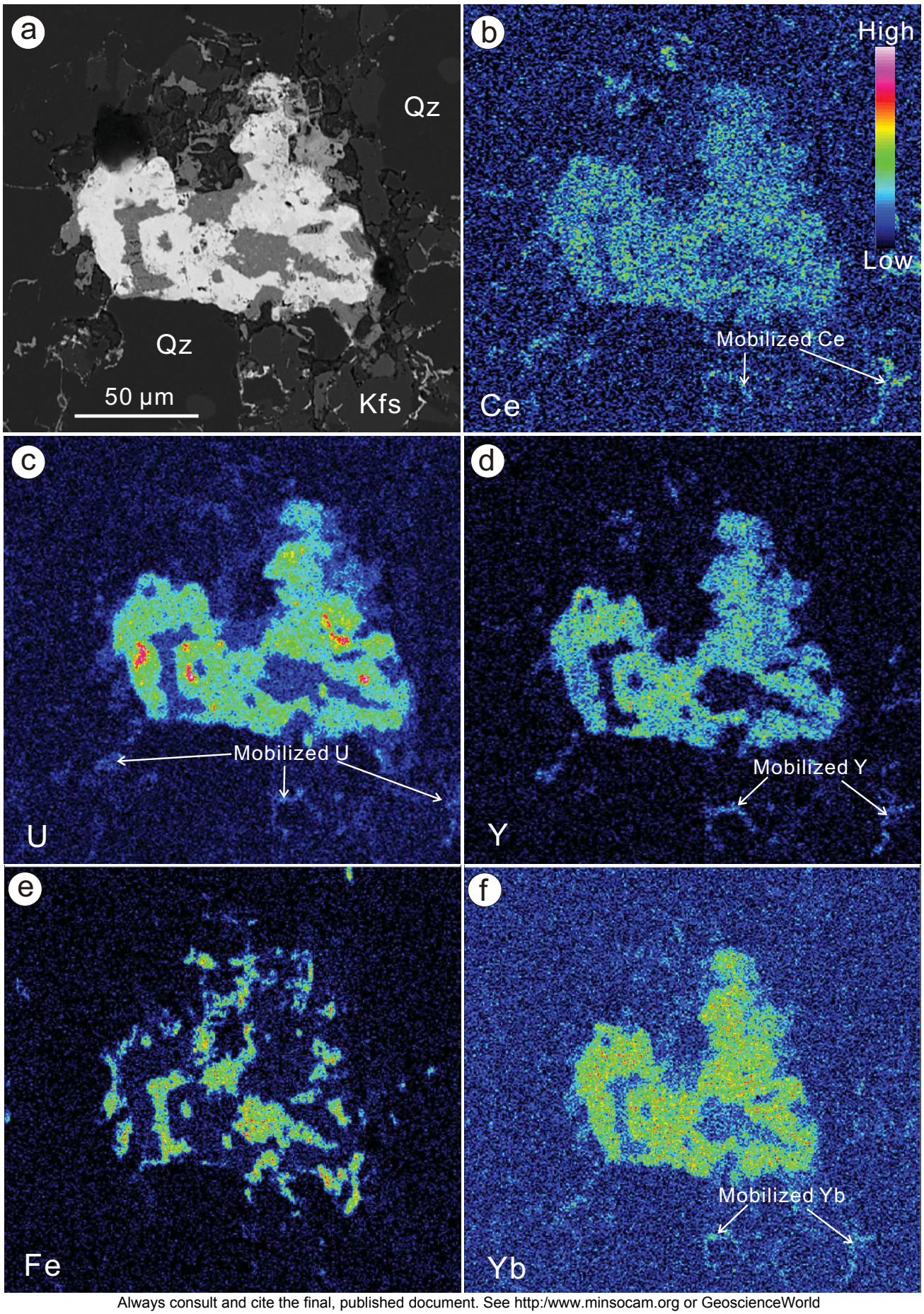

This is a preprint, the final version is subject to change, of the American Mineralogist (MSA)
Cite as Authors (Year) Title. American Mineralogist, in press.
DOI: https://doi.org/10.2138/am-2020-7383

Figure 12

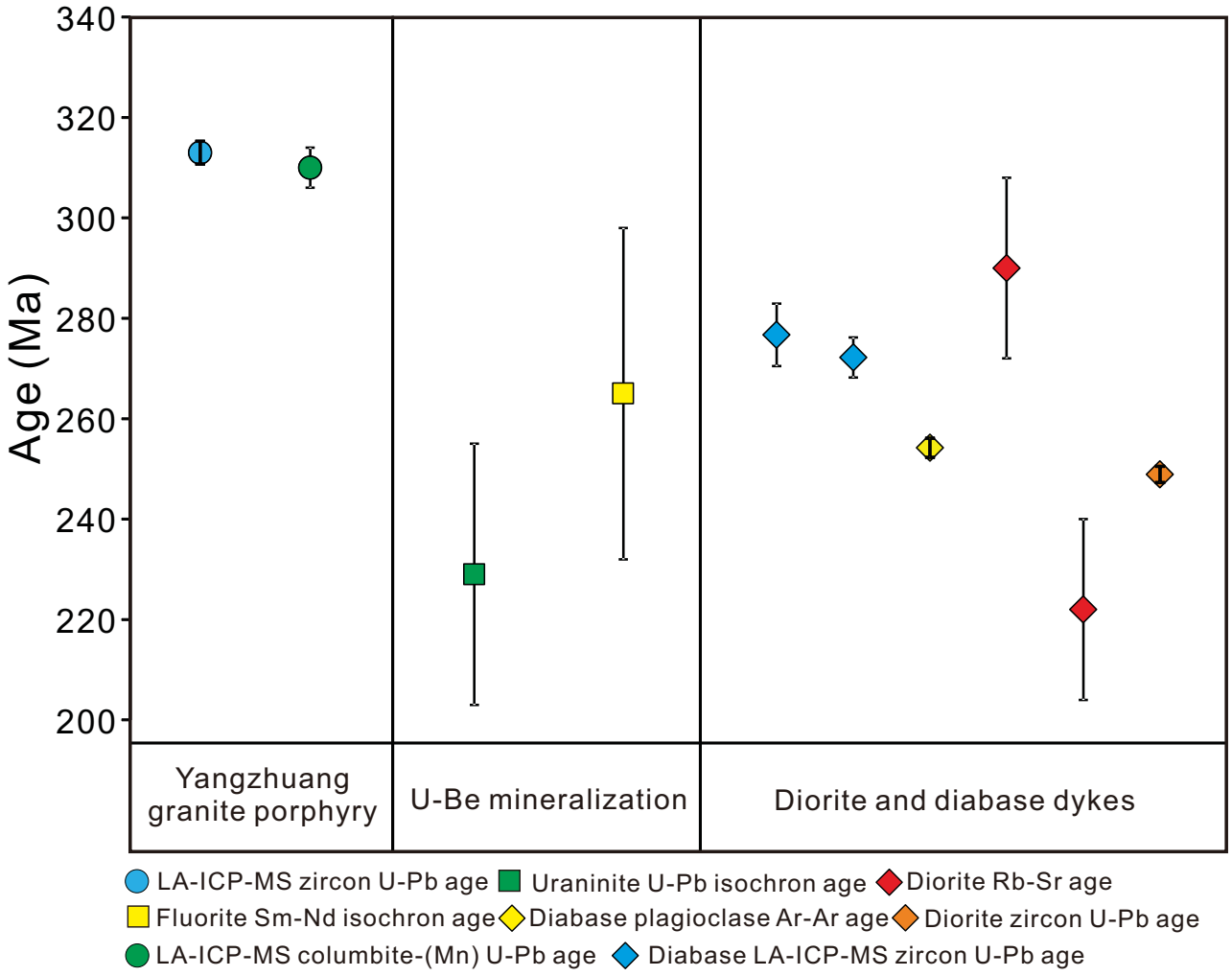

This is a preprint, the final version is subject to change, of the American Mineralogist (MSA)
Cite as Authors (Year) Title. American Mineralogist, in press.
DOI: https://doi.org/10.2138/am-2020-7383

Figure 13